

Stability of Spherical Vesicles in Electric Fields

Tetsuya Yamamoto,* Said Aranda-Espinoza, Rumiana Dimova, and Reinhard Lipowsky

Theory & Bio-Systems, Max Planck Institute of Colloids and Interfaces, 14424 Potsdam, Germany

Received March 19, 2010. Revised Manuscript Received May 26, 2010

The stability of spherical vesicles in alternating (ac) electric fields is studied theoretically for asymmetric conductivity conditions across their membranes. The vesicle deformation is obtained from a balance between the curvature elastic energies and the work done by the Maxwell stresses. The present theory describes and clarifies the mechanisms for the four types of morphological transitions observed experimentally on vesicles exposed to ac fields in the frequency range from 500 to 2×10^7 Hz. The displacement currents across the membranes redirect the electric fields toward the membrane normal to accumulate electric charges by the Maxwell–Wagner mechanism. These accumulated electric charges provide the underlying molecular mechanism for the morphological transitions of vesicles as observed on the micrometer scale.

1. Introduction

The interactions of biological cells and electromagnetic fields can be viewed from two different perspectives. On the one hand, one would like to ensure that living cells, including those of our body, are not damaged by continuous exposure to various types of electromagnetic fields generated by power transmission lines, home appliances, and electronics for telecommunications. On the other hand, electromagnetic fields can also be applied deliberately to manipulate biological cells in various ways.^{1,2} Indeed, cells exhibit various responses to electric fields such as dielectrophoresis,² electrodeformation,^{3–6} electroporation (electroporation), and electrofusion^{1,7,8} depending on the cell types and the electric fields used in the experiments. Therefore, electric fields provide experimental tools to perturb and manipulate cells and are potentially useful in characterizing their mechanical and electrical properties.^{3,4,9}

The fundamental structure of cell membranes is provided by lipid bilayers, which assemble spontaneously in aqueous solutions and can form giant vesicles with a linear size on the order of 10–100 μm (i.e., the typical size of biological cells). Because giant vesicles can be directly observed by optical microscopy, they provide useful model systems for the interactions of biological membranes with electric fields.¹⁰ Indeed, the method of electroformation,¹¹ in which lipid films are swollen under the influence of electric fields, is widely used to prepare giant unilamellar vesicles, even though the underlying mechanisms are not fully understood.¹²

In alternating (ac) electric fields, vesicles are deformed into various shapes depending on the frequency and the conductivities, σ_{in} and σ_{ex} , of the interior and the exterior solutions, respectively. Most of the earlier studies have been devoted to vesicles with identical conductivities on both sides of the membrane i.e., $\sigma_{\text{in}} = \sigma_{\text{ex}}$. In this case, external ac electric fields deform spherical vesicles into prolates at low frequencies in the range of 1–3 kHz.¹³ Theoretically, Winterhalter and Helfrich¹⁴ determined the shapes of vesicles in ac electric fields from the competition between the curvature elastic energies and the work done by the Maxwell stresses. The vesicles were modeled as lossy dielectrics, and the electric field distributions were calculated in terms of the conductivities and the dielectric constants of the membrane and the solutions. In ref 14, the vesicles always exhibited prolate deformations in the presence of ac electric fields, but possible effects arising from the asymmetry in the conductivities of the two aqueous solutions (i.e., $\sigma_{\text{in}} \neq \sigma_{\text{ex}}$) have not been taken into account.

Recently, our group reported the morphological diagram of vesicles in ac electric fields over a wide range of field frequencies and conductivity ratios $\sigma_{\text{in}}/\sigma_{\text{ex}}$.^{15,16} Henceforth, we denote this ratio as

$$\chi \equiv \sigma_{\text{in}}/\sigma_{\text{ex}} \quad (1)$$

The morphological diagram and two typical examples of vesicle deformation are shown in Figure 1. Four types of morphological transitions were observed. Among them, the prolate–oblate morphological transition for $\chi < 1$ (i.e., transition 4 in Figure 1) was discovered for the first time in this experiment. Mitov et al.¹⁷ also reported that vesicles in purified water exhibit the prolate–oblate transition, but the key role played by the asymmetric conductivity conditions has not been elucidated. Vesicles can assume spherocylindrical morphologies (e.g., tubelike and disk-like shapes) when exposed to dc pulses. However, these shapes are transient structures and are observable only for a few milliseconds.¹⁰ In this paper, we focus on the physical mechanisms underlying the morphological transitions between the stationary shapes of

*To whom correspondence should be addressed. E-mail: tetsujava@hotmail.com.

(1) Neumann, E.; Sowers, A. E.; Jordan, C. A. *Electroporation and Electrofusion in Cell Biology*; Plenum Press: New York, 1989.

(2) Zimmermann, U.; Neil, G. A. *Electromanipulation of Cells*; CRC Press: Boca Raton, FL, 1996.

(3) Engelhardt, H.; Gaub, H.; Sackmann, E. *Nature* **1984**, *307*, 378–380.

(4) Engelhardt, H.; Sackmann, E. *Biophys. J.* **1988**, *54*, 495–508.

(5) Takashima, S.; Asakura, T. *Science* **1983**, *220*, 411.

(6) Takashima, S.; Chang, S.; Asakura, T. *Proc. Nat. Acad. Sci. U.S.A.* **1985**, *22*, 6860.

(7) Chang, D. C.; Chassy, B. M.; Saunders, J. A.; Sowers, A. E. *Guide to Electroporation and Electrofusion*; Academic Press: San Diego, 1992.

(8) Lewis, T. J. *IEEE Trans. Dielectr. Electr. Insul.* **2003**, *10*, 769.

(9) Voldman, J. *Annu. Rev. Biomed. Eng.* **2006**, *8*, 425.

(10) Dimova, R.; Riske, K. A.; Aranda, S.; Bezlyepkina, N.; Knorr, R. L.; Lipowsky, R. *Soft Matter* **2007**, *3*, 817–827.

(11) Angelova, M. I.; Dimitrov, D. S. *Faraday Discuss.* **1986**, *81*, 303–311.

(12) Angelova, M. I. In *Giant Vesicles*; Luisi, P., Walde, P., Eds.; Wiley: Chichester, U.K., 2000; Chapter 3, pp 27–43.

(13) Kummrow, M.; Helfrich, W. *Phys. Rev. A* **1991**, *44*, 8356–8360.

(14) Winterhalter, M.; Helfrich, W. *J. Colloid Interface Sci.* **1988**, *122*, 583–586.

(15) Aranda, S.; Riske, K. A.; Lipowsky, R.; Dimova, R. *Biophys. J.* **2008**, *95*, L19–L21.

(16) Aranda, S. *Deformation of Model Membranes Subjected to Electric Fields*. Ph.D. Thesis, University of Potsdam, 2009.

(17) Mitov, M. D.; Méléard, P.; Winterhalter, M.; Angelova, M. I.; Bothorel, P. *Phys. Rev. E* **2007**, *19*, 628–631.

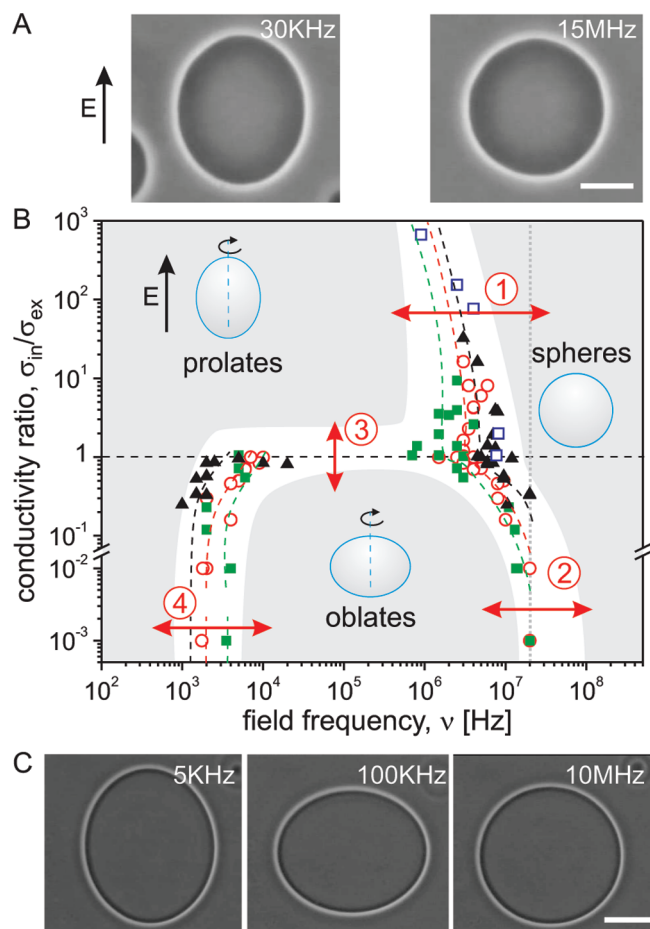


Figure 1. Morphological diagram of giant vesicles in ac electric fields (B) and examples of vesicle deformation under two conductivity conditions (A) $\sigma_{in}/\sigma_{ex} = 4.64$ and (C) $\sigma_{in}/\sigma_{ex} = 0.5$. (B) The vertical axis is the ratio σ_{in}/σ_{ex} of the conductivity σ_{in} of the interior solution with respect to the conductivity σ_{ex} of the exterior solution. The horizontal axis is the frequency ν of the electric field (i.e., the angular frequency ω divided by 2π). The conductivity σ_{ex} is varied, but σ_{in} is fixed at 1.5 (■), 6.5 (○), 13 (▲), and 1000 mS/m (□). The data were collected for a field strength of magnitude 0.2 kV/cm. The broken lines are a guide to the eye, and the shaded areas indicate zones of specific morphology. The limit of the experimentally accessible frequency, 2×10^7 Hz, is indicated by the gray dotted vertical line. The scale bars in A and C correspond to 10 μ m.

vesicles in ac electric fields; the transient shapes of vesicles in dc pulses are beyond the scope of our study.

A couple of theoretical efforts have been made to understand the mechanisms of prolate–oblate morphological transitions. Peterlin et al.¹⁸ extended the Winterhalter–Helfrich model by taking into account the anisotropy of the dielectric constant of the membranes and predicted prolate–oblate morphological transitions. However, because these transitions are observed only for $\chi < 1$ in the experiments, the underlying mechanisms should be connected to the asymmetrical conductivity condition, $\sigma_{in} \neq \sigma_{ex}$, across the membranes. An electromechanical coupling model^{19–21} has been motivated by the analogy between membranes and liquid crystals.^{22,23}

Gao et al. analyzed the stability of the vesicle in constant (dc) electric fields and found that an asymmetry in the dielectric constants between the interior and the exterior of vesicles may induce the instability of spherical vesicles.²¹ Such a mechanism is, however, unlikely to be effective in the systems studied here because the dielectric constants are not sensitive to the salt concentrations in the aqueous solutions.²⁴ Instead, the asymmetry in the conductivity condition should rather be the main driving force for the morphological transitions considered here. Vlahovska et al.²⁵ constructed an electrohydrodynamic model of vesicle deformations extending the theory of droplets in ac electric fields.²⁶ The shapes of the vesicles were derived from the mechanical balance of the elastic stresses, the viscous stresses, the tensions, and the Maxwell stresses, and the prolate–oblate morphological transitions were predicted numerically. However, the focus of the electrohydrodynamic theory was on possible hydrodynamic flows driven by ac electric fields and the electric field distributions, and Maxwell stresses were not analyzed in detail. Rey et al. performed finite element calculations by taking into account the asymmetric conductivity conditions.²⁸ The prolate–oblate morphological transitions were not predicted by their theory, presumably because the insulating properties of the membrane were not fully implemented in the boundary conditions. These previous studies suggest that we need to perform a careful analysis of the electric field distributions around the membrane under asymmetric conductivity conditions in order to clarify the mechanisms underlying the morphological transitions.

In this paper, we analyze the stability of spherical vesicles in ac electric fields to elucidate these mechanisms. Instead of taking into account all possible contributions to the vesicle deformations and performing numerical calculations as in refs 25 and 28, the objective of our paper is to construct the morphological diagram analytically and to clarify the physical mechanisms underlying the morphological transitions. Some preliminary results of the present theory were briefly reported in an earlier review.²⁹ The Winterhalter–Helfrich calculation is extended to asymmetric conductivity conditions and to a wide range of frequencies. The free energy of the system is constructed as the sum of the curvature elastic energy and the work done by the Maxwell stresses. The shapes of the vesicles are determined by minimizing the free energy. We analyzed the vesicle deformation for three frequency regimes corresponding to low, intermediate, and high frequencies. In this way, the four types of morphological transitions in Figure 1, including the prolate–oblate transition, are obtained within a unified theoretical description. The displacement currents across the membrane act to redirect the electrical fields towards the membrane normal and to accumulate electrical charges via the so-called Maxwell–Wagner mechanism.^{30,31} The electric forces arising from the interactions between the accumulated electric charges and the electric fields drive the prolate–oblate morphological transitions. We analyze the Maxwell equations in the quasistatic approximation and emphasize the physical mechanisms underlying the morphological transitions. The prolate–oblate transitions are shown to be governed by the

(24) Nörtemann, K.; Hilland, J.; Kaatz, U. *J. Phys. Chem. A* **1997**, *101*, 6864–6869.

(25) Vlahovska, P. M.; Gracià, R. S.; Aranda-Espinoza, S.; Dimova, R. *Biophys. J.* **2009**, *96*, 4789–4803.

(26) Taylor, G. *Proc. R. Soc. London, Ser. A* **1996**, *291*, 159–166.

(27) Grosse, C.; Schwan, H. P. *Biophys. J.* **1992**, *63*, 1632–1642.

(28) Rey, J. I.; Connolly, R. J.; Jaroszeski, M. J.; Hoff, A. M.; Llewellyn, J. A.; Gilbert, R. *IEEE Trans. Dielectr. Electr. Insul.* **2009**, *16*, 1280.

(29) Dimova, R.; Bezlyepkina, N.; Jordo, M. D.; Knorr, R. L.; Riske, K. A.; Staykova, M.; Vlahovska, P. M.; Yamamoto, T.; Yang, P.; Lipowsky, R. *Soft Matter* **2009**, *5*, 3201–3212.

(30) Maxwell, J. C. *A Treatise on Electricity and Magnetism*, 3rd ed.; Clarendon Press: Oxford, 1891 Vol. 1, Chapter 9.

(31) Wagner, K. W. *Arch. Electrotech.* **1914**, *2*, 371.

(18) Peterlin, P.; Svetina, S.; Žeks, B. *J. Phys. Condens. Matter* **2007**, *19*, 136220.

(19) Rey, A. D. *Phys. Rev. E* **2006**, *74*, 011710.

(20) Gao, L. T.; Feng, X. Q.; Gao, H. J. *Comput. Phys.* **2009**, *228*, 4162.

(21) Gao, L.; Liu, Y.; Qin, Q. H.; Feng, X. Q. *Acta Mech. Sin.* **2010**, *26*, 5.

(22) Petrov, A. G. *Mol. Cryst. Liq. Cryst.* **1999**, *332*, 577.

(23) Ou-Yang, Z. C.; Liu, J. X.; Xie, Y. Z. *Geometric Methods in the Elastic Theory of Membranes in Liquid Crystal Phases*; World Scientific: Singapore, 1999.

redirection of the electric fields and by the interplay between vesicle geometry and displacement currents.

This paper is organized as follows. The experimental results for the morphologies of giant vesicles in ac electric fields are briefly summarized in section 2. Our theoretical approach is described in section 3. Sections 4 and 5 are devoted to the morphological diagram. The asymptotic expressions of the amplitudes of the vesicle deformation are derived for three frequency regimes, and the morphological diagram is theoretically deduced in section 4. In section 5, we perform a global stability analysis for all frequencies. In sections 6 and 7, we emphasize the physical mechanisms underlying the morphological transitions of the vesicle and analyze the morphological transitions in terms of the electric charges accumulated at the vesicle membrane. The force densities associated with the Maxwell stresses are reinterpreted as force densities arising from the interplay between electric fields and accumulated electric charges in section 6. The mechanism of the morphological transition is discussed on the basis of the reinterpretation in section 7, and the present theory is compared with the electrohydrodynamic model²⁵ and the experiments in section 8, followed by our conclusions in section 9.

2. Experiment

In this section, we briefly summarize the experimental results for the morphological transitions of vesicles exposed to ac electric fields as reported in refs 15 and 29.

Giant unilamellar vesicles were prepared from conventional egg yolk L- α -phosphatidylcholine (Avanti Polar Lipids, Alabaster, AL) in NaCl solutions by the electroformation method.¹¹ The details of the preparation procedures are described in the Supporting Information of ref 15. The vesicle dispersions were subsequently diluted in isotonic NaCl solutions with different concentrations to achieve asymmetric conductivity conditions. The salt concentrations of the exterior and interior solutions were varied systematically between 0.01 and 100 mM to study a wide range of conductivity ratio χ . During the preparation, sucrose and glucose were dissolved in the interior and exterior solutions, respectively, in order to enhance the optical contrast due to the different refractive indices of these solutions. The observed vesicles had radii of between 4 and 50 μm . The vesicles were placed between two cylindrical electrodes in the working chamber (Eppendorf, Germany) and then observed through a phase-contrast microscope (Zeiss, Germany). The vesicles experienced dielectrophoresis for ac electric fields in the frequency range below 1 kHz. For larger frequencies, the dielectrophoretic movements were small and could be ignored.

The vesicle morphologies depend primarily on the angular frequency $\omega = 2\pi\nu$, where ν is the experimental frequency of the ac field as well as for the ionic conductivities σ_{in} and σ_{ex} of the interior and exterior vesicle compartments, respectively. The conductivity ratio χ , which is defined by eq 1, has been experimentally varied between 10^{-3} and 10^3 . Figure 1 summarizes the observed morphologies as a function of the frequency ν and conductivity ratio χ . The conductivities of the interior solutions were fixed at 1.5 mS/m in the data set plotted with filled squares, 6.5 mS/m in the plot with open circles, 13 mS/m in the plot with filled triangles, and 1000 mS/m in the plot with open squares. The broken lines are just a guide for the eye, and the shaded areas indicate zones of specific morphology. The limit of the experimentally accessible frequency, which is 2×10^7 Hz, is indicated by the gray dotted vertical line. The vesicles exhibited four types of morphological transitions. At high frequency, the vesicles assume a spherical shape that is independent of the conductivity ratio χ . For $\chi > 1$, the vesicles were deformed into prolates at ~ 1 –10 MHz upon decreasing the frequency (i.e., transition 1 in Figure 1). The prolate vesicles did not exhibit further morphological transitions when decreasing the frequency while keeping χ constant. However,

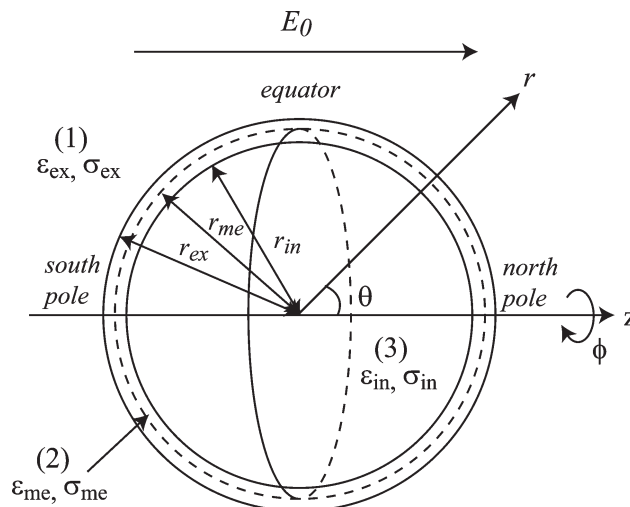


Figure 2. Geometry of a spherical vesicle in ac electric fields. The vesicle is modeled as a spherical shell of lossy dielectrics with dielectric constant ϵ_{me} and conductivity σ_{me} . The ac electric fields are applied to the vesicle in the z direction. A spherical coordinate system, where r is the distance from the center of the vesicle, θ is the inclination angle, and ϕ is the azimuthal angle, is used. The interior of the vesicle is filled with a solution characterized by dielectric constant ϵ_{in} and conductivity σ_{in} . The exterior solution has dielectric constant ϵ_{ex} and conductivity σ_{ex} . The parameters r_{ex} and r_{in} are the exterior and interior radii of the vesicle. The radius of the vesicle is defined by $r_{\text{me}} \equiv r_{\text{in}} + l_{\text{me}}/2$.

for $\chi < 1$, the spherical vesicles were deformed into oblates at ~ 10 MHz upon decreasing the frequency (i.e., transition 2). The vesicles adopted oblate shapes in the frequency range from ~ 10 MHz to ~ 1 kHz. Further decrease in the frequency changed the shapes of the vesicles into prolate at ~ 1 –10 kHz (i.e., transition 4). The vesicles did not show further morphological transitions at lower frequencies. In the intermediate frequency range, the shapes of the vesicles were oblate for $\chi < 1$ and prolate for $\chi > 1$. Thus, the vesicle undergoes a prolate–oblate morphological transition with increasing χ at constant frequency; see transition 3 in Figure 1B. Figure 1A,C shows the vesicles that were subjected to electric fields of magnitude 0.2 kV/cm. The amplitude of the deformation increases with magnitude E_0 of the electric field; however, the morphologies of the vesicles are not affected by E_0 , at least not for $E_0 < 0.2$ kV/cm.

The experimental results show that the morphologies of the giant vesicles are sensitive to the conductivities of the solutions and the frequency. In the Maxwell theory of electrodynamics, the currents flowing in a system are provided by the conduction currents and the displacement currents, which are proportional to the conductivity and the frequency, respectively. The two types of electric currents determine the distributions of the electric fields, which are the origin of the Maxwell stresses deforming the vesicle. On the basis of this observation, we construct a theory of morphological transitions of the vesicles in ac electric fields and focus on the electric currents flowing through the system in the following sections.

3. Theoretical Description

3.1. Geometry of the System. Because we consider vesicles that can be resolved by optical microscopes and thus have lateral dimensions of many micrometers, the vesicle membrane is regarded as a thin sheet of constant thickness l_{me} . Let us consider a vesicle that attains a spherical shape in the absence of the ac electric fields; see Figure 2. It is convenient to use a spherical coordinate system with radial coordinate r , inclination angle θ , and azimuthal angle ϕ . The spherical vesicle has an interior radius

r_{in} and an exterior radius r_{ex} with $r_{\text{ex}} = r_{\text{in}} + \ell_{\text{me}}$. The radius of the spherical vesicle is defined by

$$r_{\text{me}} \equiv r_{\text{in}} + \frac{\ell_{\text{me}}}{2} \quad (2)$$

see Figure 2.

Far away from the vesicles, the ac electric fields are taken to have a constant direction that defines the Cartesian coordinate z ; see Figure 2. The experimentally observed deformations of the vesicles arising from these fields (section 2) are small compared to the vesicle radius r_{me} . The deformed vesicle shapes can then be described by

$$\mathbf{r}(\theta, \phi) = r_{\text{me}}\mathbf{e}_r + \mathbf{u}(\theta, \phi) \quad (3)$$

with the unit vector \mathbf{e}_r in the r direction and the displacement vector \mathbf{u} that depends, in general, on both angles θ and ϕ .

3.2. Bending Energy of Small Deformations. The deformation of a vesicle by an ac electric field leads to an increase in the vesicle's bending energy. In this subsection, we calculate this energy increase following ref 14. The derivation of the bending energy increase is given in the Supporting Information. In the experiments, the spherical vesicles are deformed into prolate or oblate shapes that are axially symmetric with respect to the z axis. To describe these latter deformations, the displacement vector $\mathbf{u} = (u_r, u_\theta, u_\phi)$ is parametrized as

$$u_r = \frac{1}{2}s(3\cos^2\theta - 1) \quad (4)$$

$$u_\theta = -s\sin\theta\cos\theta \quad (5)$$

and $u_\phi = 0$ where the parameter s represents the overall deformation amplitude. The deformations into prolate and oblate are described by $s > 0$ and $s < 0$, respectively. The parametrization as given by eqs 4 and 5 conserves the local surface area of the membrane (Supporting Information), which ensures that the total membrane area stays constant during the deformation.

The deformation as given by eqs 4 and 5 leads to the excess bending energy

$$\Delta F_{\text{bc}} = \frac{48\pi}{5} \left(1 - \frac{M_{\text{sp}}r_{\text{me}}}{6}\right) \kappa \left(\frac{s}{r_{\text{me}}}\right)^2 \quad (6)$$

which depends on the bending rigidity κ and the spontaneous curvature M_{sp} of the vesicle membrane. This excess energy is proportional to the square of s , which implies that the spherical state with $s = 0$ is stable in the absence of the external electric fields.

3.3. Electric Field Distribution. The vesicle membrane is modeled as a spherical shell composed of a lossy dielectric with finite thickness ℓ_{me} . The conductivity and dielectric constant of the vesicle are denoted by σ_{me} and ϵ_{me} , respectively. The membrane separates the interior from the exterior vesicle compartment, which will be distinguished by the subscripts “in” and “ex”. Both compartments contain aqueous solutions that usually differ in their ionic concentrations. The specific conductivity and the dielectric constant of the interior solution are denoted by σ_{in} and ϵ_{in} , and those of the exterior are denoted by σ_{ex} and ϵ_{ex} . In general, we will consider the asymmetric situation with $\sigma_{\text{ex}} \neq \sigma_{\text{in}}$. The two membrane surfaces in contact with the two solutions represent the exterior and interior interfaces. For the spherical vesicle, the exterior and interior interfaces are located r_{ex} and r_{in} from the center of the vesicle, respectively; see Figure 2.

The applied ac electric field, which is uniform far away from the vesicle, is characterized by the (angular) frequency ω and is directed to the unit vector \mathbf{e}_z . This spatially uniform field has

the form

$$\mathcal{E}_0(t) = \frac{1}{2}E_0\mathbf{e}^{-i\omega t}\mathbf{e}_z + \text{cc} \quad (7)$$

where cc stands for “complex conjugate”. In the following text, we will always use the frequency ω apart from Figures 1 and 7 that contain plots as functions of $\nu \equiv \omega/2\pi$.

For the whole frequency range studied experimentally (Figure 1), the wavelength of the ac electric fields was very large compared to the size of the vesicles. This separation of length scales implies that we can use the so-called quasistatic approximation to the Maxwell equations. The fundamental equations and the boundary conditions for the electric fields in the latter approximation are summarized in the Supporting Information. In the quasistatic approximation, one omits the time derivative of the magnetic field, which implies $\nabla \times \mathbf{E} = 0$. Furthermore, because the observed deformations of the vesicle shapes are quite small compared to the vesicle radii, we will calculate the electric field distribution for the undeformed spherical shapes.

Expression 7 represents the electric field distribution when the chamber contains no vesicle. In the presence of such a vesicle, the field distribution has the general form

$$\mathcal{E}_k(r, \theta, t) = \frac{1}{2}\mathbf{E}_k(r, \theta)\mathbf{e}^{-i\omega t} + \text{cc} \quad (8)$$

with $k = 1, 2$, and 3 . Here and below, subscripts 1, 2, and 3 stand for subscripts ex, me, and in and thus denote the exterior solution, the membrane, and the interior solution, respectively. The quantity $\mathbf{E}_k(r, \theta)$ represents the time-independent part of the electric fields. Because $\nabla \times \mathbf{E} = 0$ is satisfied in the quasistatic approximation, it is possible to define scalar potentials $U_k(r, \theta)$ with $k = 1, 2$, and 3 , which satisfy the Laplace equation

$$\nabla^2 U_k(r, \theta) = 0 \quad (9)$$

The electric fields $\mathbf{E}_k(r, \theta)$ are then obtained via $\mathbf{E}_k(r, \theta) = -\nabla U_k(r, \theta)$. The solutions of eq 9, which approach eq 7 far away from the vesicle, have the form³²

$$U_k(r, \theta) = -E_k^c r \cos\theta + \frac{\mu_k \cos\theta}{r^2} \quad (10)$$

with $k = 1, 2$, and 3 . Note that the first and second terms in eq 10 have the form of the electric potentials arising from constant electric fields in the z direction and from image dipoles located at the center of the vesicle, respectively. Amplitudes E_k^c and μ_k for $k = 1, 2$, and 3 are determined by the boundary conditions.

The tangential components of the electric fields and the normal components of the current densities ($\sigma_k + \epsilon_k \partial/\partial t$) \mathbf{E}_k are continuous across the two interfaces between the three media (Supporting Information). The continuity requirements lead to the boundary conditions

$$E_m \sin\theta = E_2 \sin\theta \text{ and} \quad (11)$$

$$\psi_m E_m \cos\theta = \psi_2 E_2 \cos\theta \quad (12)$$

at $r = r_{\text{ex}}$ and $r = r_{\text{in}}$ for $m = 1$ and 3 , respectively, with $E_k \equiv |E_k|$ and the admittances

$$\psi_k = \sigma_k - i\omega\epsilon_k \quad (13)$$

for the different media with $k = 1, 2$, and 3 . Amplitudes E_k^c and μ_k for $k = 1, 2$, and 3 are determined so that the electric fields $\mathbf{E}_k(r, \theta)$ satisfy eqs 11 and 12 in the interior and exterior interfaces and

(32) Jackson, J. D. *Classical Electrodynamics*; John Wiley and Sons: New York, 1962.

approach eq 7 far away from the vesicle. These amplitudes can be expressed in terms of the complex-valued parameters

$$\beta_1 \equiv \frac{\sigma_2 - i\omega\epsilon_2}{\sigma_1 - i\omega\epsilon_1} \quad (14)$$

$$\beta_3 \equiv \frac{\sigma_2 - i\omega\epsilon_2}{\sigma_3 - i\omega\epsilon_3} \quad (15)$$

and the ratio $r_{\text{in}}/r_{\text{ex}}$ of the interior to exterior radii. Parameters β_1 and β_3 represent the ratio between the membrane admittance, ψ_{me} , and the admittances of the exterior and the interior solutions, ψ_{ex} and ψ_{in} , respectively. The expressions for E_k^* and μ_k are given in Appendix A.

3.4. Work Performed by Maxwell Stresses. The electric fields apply Maxwell stresses at the exterior and interior interfaces of the vesicle, and the Maxwell stresses are the driving force deforming the vesicle. Maxwell stress tensors are represented as the symmetric two-rank tensors^{32,33}

$$\mathbf{T}_k(r, \theta, t) = \epsilon_k \left[\mathcal{G}_k(r, \theta, t) \mathcal{G}_k(r, \theta, t) - \frac{1}{2} \mathcal{G}_k^2(r, \theta, t) \mathbf{I} \right] \quad (16)$$

in diadic expression with $k = 1, 2$, and 3 . \mathbf{I} is an identical operator. Among the six independent components of the Maxwell stress tensor in each medium, only the rr and $r\theta$ components deform the vesicle; see Appendix B. These stress components take the forms

$$T_{kr}(r, \theta, t) = \epsilon_k \left[\frac{1}{2} \mathcal{G}_{kr}^2(r, \theta, t) - \frac{1}{2} \mathcal{G}_{k\theta}^2(r, \theta, t) \right] \quad (17)$$

$$T_{k\theta}(r, \theta, t) = \epsilon_k \mathcal{G}_{kr}(r, \theta, t) \mathcal{G}_{k\theta}(r, \theta, t) \quad (18)$$

with $k = 1, 2$, and 3 . Equation 17 shows that the Maxwell stresses have tensile and compressive contributions that are driven by the normal and tangent electric fields, \mathcal{G}_{kr} and $\mathcal{G}_{k\theta}$, respectively. In the following, we denote these tensile and compressive contributions to T_{kr} as tensile and compressive Maxwell stresses. The Maxwell stresses are composed of time-dependent and time-independent terms. Stationary deformations of the vesicle are induced by the time-independent terms of the Maxwell stresses, and we omit the time-dependent terms of the Maxwell stresses in the following. The time-independent terms of the Maxwell stresses are extracted by the time average over one period, $2\pi/\omega$. Electric charges are not trapped in the membrane, and the Maxwell stresses do not produce net forces in the bulk of the membrane. Because the conductivity and dielectric constant change discontinuously across the exterior and the interior interfaces, the Maxwell stresses are also discontinuous across these interfaces (i.e., $\mathbf{T}_1(r_{\text{ex}}, \theta, t) \neq \mathbf{T}_2(r_{\text{ex}}, \theta, t)$ and $\mathbf{T}_2(r_{\text{in}}, \theta, t) \neq \mathbf{T}_3(r_{\text{in}}, \theta, t)$) and generate net force densities at the two interfaces of the vesicle. These force densities are given by

$$\mathbf{f}_{\text{ex}} = -\mathbf{n}_{\text{ex}} \cdot (\langle \mathbf{T}_2(r_{\text{ex}}, \theta, t) \rangle - \langle \mathbf{T}_1(r_{\text{ex}}, \theta, t) \rangle) \quad (19)$$

$$\mathbf{f}_{\text{in}} = -\mathbf{n}_{\text{in}} \cdot (\langle \mathbf{T}_2(r_{\text{in}}, \theta, t) \rangle - \langle \mathbf{T}_3(r_{\text{in}}, \theta, t) \rangle) \quad (20)$$

respectively. The angular brackets indicate the average in time over one time period. The unit vectors $\mathbf{n}_{\text{ex}} \equiv \mathbf{e}_r$ and $\mathbf{n}_{\text{in}} \equiv -\mathbf{e}_r$ are the outward normal vectors of the exterior and interior interfaces.

Associated with the deformations, the force densities perform the work

$$W_{\text{el}} = \int dA_{\text{ex}} \mathbf{f}_{\text{ex}} \cdot \mathbf{u} + \int dA_{\text{in}} \mathbf{f}_{\text{in}} \cdot \mathbf{u} \quad (21)$$

where dA_{ex} and dA_{in} are area integrals over the exterior and the interior interfaces, respectively. The explicit expression of W_{el} is given by eq 92 in Appendix B. Because \mathbf{f}_{ex} and \mathbf{f}_{in} are independent of the deformation amplitudes s whereas \mathbf{u} is proportional to s (eqs 4 and 5), the work W_{el} done by the Maxwell stresses is linear with respect to s (eqs 93 and 94).

3.5. Free Energy of Vesicles in ac Electric Fields. The free energies of the vesicles in the external ac electric fields are represented as

$$F = \Delta F_{\text{be}} - W_{\text{el}} \quad (22)$$

The excess bending energies ΔF_{be} are proportional to the square of s (eq 6), whereas the work, W_{el} , done by the Maxwell stresses is linear with respect to s (eqs 93 and 94). The stable shapes of the vesicles are determined to minimize the free energies with respect to s . In the absence of an external electric field $E_0 = 0$, the spherical shape with $s = 0$ achieves the minimum in the free energies. The deformation amplitudes s of the free-energy minimum shift to positive or negative values depending on the sign of the work W_{el} done by the Maxwell stresses. The prolate shape is stable when the free-energy minimum shifts to positive, $s > 0$, whereas the oblate shape is stable when the free-energy minimum shifts to negative, $s < 0$.

4. Analysis for Different Frequency Regimes

The optimal amplitudes of the deformation are derived by finding the minimum in the free energies represented by eq 22. However, the work W_{el} done by the Maxwell stresses is a complex function of the (angular) frequency, ω , and the ratio between the interior and the exterior radii, $r_{\text{in}}/r_{\text{ex}}$; see Appendix B. Thus, in this section, we derive simple asymptotic expressions of W_{el} in low-, intermediate-, and high-frequency regimes and analyze the stabilities of the spherical vesicle in ac electric fields.

The stable shape of the vesicle is determined by the sign of the work W_{el} done by the Maxwell stresses, and it is determined by β_1 , β_3 , and $r_{\text{in}}/r_{\text{ex}}$; see Appendix B. Indeed, β_1 and β_3 are rather small quantities (i.e., $|\beta_1| \ll 1$ and $|\beta_3| \ll 1$) because the conductivity of the membrane is orders of magnitude smaller than the conductivities of the solutions and the dielectric constant of the membrane is one order of magnitude smaller than the dielectric constant of the solutions. The estimates of the physical quantities involved are summarized in the Supporting Information. Since the thickness l_{me} of the bilayer membrane is orders of magnitudes smaller than the exterior radius r_{ex} of the vesicle, it is convenient to define the ratio of the two length scales

$$\delta \equiv \frac{l_{\text{me}}}{r_{\text{ex}}} \quad (23)$$

whose order of magnitude is 10^{-4} for giant vesicles with a linear size of $10 \mu\text{m}$.

β_1 and β_3 increase with frequency ω whereas δ is independent of frequency ω . In other words, the frequency ω plays a role in changing the magnitudes of β_1 and β_3 relative to δ . In this section, we analyze eq 22 for the (i) low-frequency regime, $|\beta_1|/\delta \ll 1$ and $|\beta_3|/\delta \ll 1$, (ii) intermediate-frequency regime, $|\beta_1|/\delta \approx 1$ and $|\beta_3|/\delta \approx 1$, and (iii) high-frequency regime, $|\beta_1|/\delta \gg 1$ and $|\beta_3|/\delta \gg 1$. For simplicity, we assume that the dielectric constants of the exterior and interior solutions, ϵ_{ex} and ϵ_{in} , are equal to the dielectric constant ϵ_w of water (i.e., $\epsilon_{\text{ex}} = \epsilon_{\text{in}} = \epsilon_w$) in this section.

4.1. Low-Frequency Regime. For the typical parameters used in the experiments in section 2, the range of the low-frequency regime is approximately represented as $\omega \ll \delta\sigma_{\text{ex}}/\epsilon_{\text{me}}$ and $\omega \ll \delta\sigma_{\text{in}}/\epsilon_{\text{me}}$. $\delta\sigma_{\text{ex}}/\epsilon_{\text{me}}$ and $\delta\sigma_{\text{in}}/\epsilon_{\text{me}}$ are approximately 6 kHz for $\delta \approx 10^{-4}$, $\sigma_{\text{ex}} \approx \sigma_{\text{in}} \approx 10^{-3} \text{ S/m}$, and $\epsilon_{\text{me}} \approx 2\epsilon_0$, where ϵ_0 is the dielectric constant of vacuum. The asymptotic expression of W_{el} is

(33) Landau, L. D. Lifshitz, E. M. *Electrodynamics of Continuous Media*, 2nd ed.; Pergamon Press: Oxford, U.K., 1984.

derived by expanding eq 92 in Appendix B as

$$W_{el} \approx \frac{3\pi}{10} r_{ex}^2 s E_0^2 \epsilon_w \left[1 + \frac{Re\beta_1}{\delta} \right] \quad (24)$$

by the first-order correction with respect to β_1/δ and β_3/δ . $Re\beta_1$ is the real part of β_1 . Indeed, there are other first-order terms that are smaller than the terms represented in eq 24 by the factor of ϵ_{me}/ϵ_w ; however, we omit those terms assuming that $\epsilon_{me}/\epsilon_w \ll 1$. The optimal amplitude s of deformation is determined to minimize the total free energy as

$$\frac{s}{r_{me}} \approx \frac{1}{64} \frac{r_{me}^3 \epsilon_w}{\kappa (1 - \frac{M_{sp} r_{me}}{6})} E_0^2 \left[1 + \frac{Re\beta_1}{\delta} \right] \quad (25)$$

Because the thickness of the membrane is much smaller than the external radius, the factor of $r_{ex}^2 r_{me}^2$ is approximately represented as r_{me}^4 in the last expression. Indeed, the amplitude s of the deformation is independent of β_3 in the low-frequency regime. Because the second term in the square brackets of eq 25 is only a small correction to the first term (i.e., $Re\beta_1/\delta \ll 1$), the optimal amplitude s of deformation is positive regardless of the conductivity condition. In other words, in the low-frequency ac electric fields $\omega < 6$ kHz, the stable shape of the vesicle is prolate independent of the exterior and the interior conductivities, which is in agreement with the experimental results shown in section 2. The physical picture extracted from this analysis is described in section 7.1. For the symmetric conductivity condition (i.e., $\beta_1 = \beta_3$), eq 25 is reduced to the corresponding equation in Winterhalter–Helfrich theory; see eq 21 in ref 14.

4.2. Intermediate Frequency Regime. In the intermediate-frequency regime, β_1 and β_3 are of the same order of magnitude as δ . For typical experimental parameters, the frequency is on the order of $\delta\sigma_{ex}/\epsilon_{me}$ and $\delta\sigma_{in}/\epsilon_{me}$ in this regime. ($\delta\sigma_{ex}/\epsilon_{me}$ and $\delta\sigma_{in}/\epsilon_{me}$ are approximately 6 kHz.) The prolate–oblate morphological transitions (transition 4 in Figure 1) lie in the intermediate-frequency regime. The asymptotic expression of the work W_{el} done by the Maxwell stresses is derived as

$$W_{el} \approx \frac{6\pi}{5} r_{ex}^2 s E_0^2 \epsilon_w \frac{|\beta_1|^2 - 3|\beta_3|^2 + 2\delta(Re\beta_1 + Re\beta_3) + \delta^2 + \beta_1^* \beta_3 + \beta_1 \beta_3^*}{|2\beta_3 + \beta_1 + 2\delta|^2} \quad (26)$$

by expanding eq 92 with respect to β_1 , β_3 , and δ . For the typical parameters in the experiments and a field frequency on the order of kilohertz, at which the prolate–oblate transitions have been observed, $\delta Re\beta_1$ and $\delta Re\beta_3$ are much smaller than the other terms in eq 26. The magnitude of deformation s is approximately represented for $\chi > 1$ as

$$\frac{s}{r_{me}} \approx \frac{1}{32} \frac{r_{me}^3 \epsilon_w}{\kappa \left[1 - \frac{M_{sp} r_{me}}{6} \right]} E_0^2 \frac{1 + \frac{\omega^2}{\omega_p^2}}{1 + \frac{\omega^2}{\omega_o^2}} \quad (27)$$

with

$$\omega_p^2 = -\frac{\sigma_{in}^2 \delta^2}{\epsilon_{me}^2} \frac{1}{3 - \chi^2 - 2\chi} \quad (28)$$

$$\omega_o = \frac{\delta \sigma_{in}}{\epsilon_{me}} \frac{2}{\chi + 2} \quad (29)$$

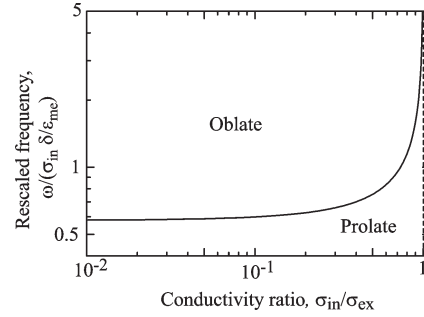


Figure 3. Dependence of the rescaled frequency $\omega/(\sigma_{in}\delta/\epsilon_{me})$ for prolate–oblate transitions on the conductivity ratio $\chi = \sigma_{in}/\sigma_{ex}$ between the interior and the exterior solutions for $\chi < 1$ as evaluated by eq 31. The angular frequency ω of the electric fields is rescaled by the interior conductivity σ_{in} , the dielectric constant ϵ_{me} of the membrane, and $\delta \equiv l_{me}/r_{ex}$ (i.e., the ratio of the membrane thickness l_{me} to the vesicle radius r_{ex}).

and for $\chi < 1$ as

$$\frac{s}{r_{me}} \approx \frac{1}{32} \frac{r_{me}^3 \epsilon_w}{\kappa \left[1 - \frac{M_{sp} r_{me}}{6} \right]} E_0^2 \frac{1 - \frac{\omega^2}{\omega_c^2}}{1 + \frac{\omega^2}{\omega_o^2}} \quad (30)$$

with

$$\omega_c^2 = \frac{\sigma_{in}^2 \delta^2}{\epsilon_{me}^2} \frac{1}{3 - \chi^2 - 2\chi} \quad (31)$$

χ is the conductivity ratio σ_{in}/σ_{ex} , which is defined in eq 1 and is the vertical axis of the morphological diagram; see Figure 1.

When the interior solution has a higher conductivity than the exterior solution (i.e., $\chi > 1$), the optimal amplitudes s of deformation are positive in this frequency regime. However, when the conductivity of the interior solution is smaller than the conductivity of the exterior solution (i.e., $\chi < 1$), the sign of s changes from positive to negative at $\omega = \omega_c$ upon increasing the frequency of the ac electric fields. In other words, the stable shape of the vesicle is prolate in the intermediate-frequency regime for $\chi > 1$ whereas the vesicle experiences prolate–oblate morphological transition at $\omega = \omega_c$ for $\chi < 1$, which is in agreement with the experiments. The predicted morphological diagram in the intermediate-frequency range is plotted in Figure 3. The present theory predicts the topology of the morphological diagram correctly. $\sigma_{in}\delta/\epsilon_{me}$ gives the typical order of the frequency for the prolate–oblate morphological transition. For the typical experimental parameters (e.g., $\sigma_{in} \approx 1$ mS/m, $\delta \approx 10^{-4}$, and $\epsilon_{me} = 2\epsilon_0$), $\sigma_{in}\delta/\epsilon_{me}$ is estimated to be 6×10^3 Hz. It roughly agrees with the order of the frequency of prolate–oblate morphological transition 4 in Figure 1. The present results demonstrate that the asymmetry of the conductivity condition plays an important role in the prolate–oblate morphological transition.

4.3. High-Frequency Regime. In the high-frequency regime, β_1 and β_3 are much larger than δ . For typical parameters used in the experiments, the frequency is much larger than $\delta\sigma_{ex}/\epsilon_{me}$ and $\delta\sigma_{in}/\epsilon_{me}$, where the latter condition is valid only for the large vesicles with $\delta \ll \epsilon_{ex}/\epsilon_{me}$. Equation 92 in Appendix B is expanded with respect to δ/β_1 and δ/β_3 . The asymptotic expression of the work W_{el} done by the Maxwell stresses is derived as

$$W_{el} \approx \frac{6\pi}{5} r_{ex}^2 s E_0^2 \epsilon_w \frac{|\beta_1|^2 - 3|\beta_3|^2 + \beta_1^* \beta_3 + \beta_1 \beta_3^*}{|2\beta_3 + \beta_1|^2} \quad (32)$$

The amplitude s of the deformation, which achieves the minimum in the free energies, is calculated as

$$\frac{s}{r_{\text{me}}} \approx \frac{1}{16} \frac{r_{\text{me}}^3 \varepsilon_w}{\kappa \left[1 - \frac{M_{\text{sp}} r_{\text{me}}}{6} \right]} E_0^2 \frac{(\sigma_{\text{in}} - \sigma_{\text{ex}})(\sigma_{\text{in}} + 3\sigma_{\text{ex}})}{(\sigma_{\text{in}} + 2\sigma_{\text{ex}})^2} \frac{1}{1 + \frac{\omega^2}{\omega_s^2}} \quad (33)$$

with

$$\omega_s = \frac{\sigma_{\text{in}} + 2\sigma_{\text{ex}}}{\varepsilon_{\text{in}} + 2\varepsilon_{\text{ex}}} = \frac{\sigma_{\text{in}} \chi + 2}{3\varepsilon_w \chi} \quad (34)$$

Equation 33 is proportional to $\sigma_{\text{ex}} - \sigma_{\text{in}}$, and the sign of the amplitude s of the deformation changes at $\chi = 1$. In other words, the stable shape of the vesicle is prolate, $s > 0$, for $\chi > 1$ and is oblate, $s < 0$, for $\chi < 1$. The amplitude of the deformation decreases gradually with the frequency ω , and eventually the vesicle returns to a spherical shape at high frequency. This corresponds to the prolate–sphere and the oblate–sphere morphological transitions observed in the experiments in section 2; see transitions 1 and 2 in Figure 1. ω_s provides the cutoff frequency for the morphological transitions between prolate or oblate to spherical shape. Indeed, ω_s corresponds to the so-called inverse Maxwell–Wagner charging time.^{30,31} We will discuss these morphological transitions on the basis of Maxwell–Wagner theory in section 7. For the typical parameters of the experiments in section 2 (e.g., $\sigma_{\text{in}} \approx 1$ mS/m and $\varepsilon_w \approx 78\varepsilon_0$), ω_s is approximately $\sigma_{\text{in}}/(3\varepsilon_w) \approx 10^6$ Hz for $\chi > 1$. The estimated value of ω_s roughly agrees with the order of the frequency at which prolate/oblate–sphere transitions were observed.

The amplitude s of the deformation decays only gradually with $1/(\omega^2 + \omega_s^2)$, and it is necessary to introduce a threshold to distinguish a sphere from a prolate or an oblate. Indeed, the distinctions between prolates/oblates and spheres in the high-frequency regime in the experiments described in section 2 were determined by whether the amplitude of the deformation is smaller or larger than the optical resolution, $0.5 \mu\text{m}$ (i.e., whether the deformation is microscopically detectable or not).¹⁶ The expression on the right hand side of eq 33 can be rewritten in the form $s/r_{\text{me}} \approx K \eta^2$ with

$$\eta^2 = \frac{|\chi - 1|(\chi + 3)}{(\chi + 2)^2} \frac{1}{1 + \frac{\omega^2}{\omega_s^2}} \quad (35)$$

where K does not depend on the frequency and the conductivities. In the experiment, s/r_{me} is measured and its threshold is defined by $0.5 \mu\text{m}/r_{\text{me}}$. The corresponding threshold η_{th} for η then follows from $K \eta_{\text{th}}^2 \approx 0.5 \mu\text{m}/r_{\text{me}}$. Thus, we define that the vesicle is a sphere when η is less than η_{th} and the vesicle is prolate or oblate when η is larger than η_{th} . At the boundary between prolate/oblate and spherical states, $\eta^2 = \eta_{\text{th}}^2$ is satisfied. In the limit of small η_{th} , the frequencies of the prolate/oblate–sphere morphological transitions are approximately given by

$$\omega_{\text{th}} \approx \frac{\sigma_{\text{in}}}{3\varepsilon_{\text{in}}\eta_{\text{th}}} \sqrt{\frac{|\chi - 1|(\chi + 3)}{\chi^2}} \quad (36)$$

The predicted morphological diagram for the high-frequency regime is plotted in Figure 4. Topologically, it is in good agreement with the experimentally determined morphological diagram; see Figure 1.

5. Global Bifurcation Analysis

In section 4, the morphological transitions of the vesicle in ac electric fields were analyzed for three frequency limits. It is interesting to verify whether the present theory predicts additional morphological transitions, which have not been detected in the experiments. The vesicle exhibits morphological transitions at the

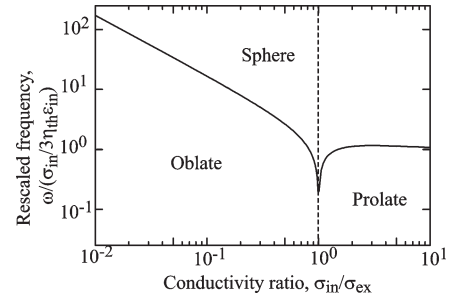


Figure 4. Dependence of the rescaled frequency, $\omega/(\sigma_{\text{in}}/3\eta_{\text{th}}\varepsilon_{\text{in}})$, for prolate/oblate–sphere transitions on the conductivity ratio $\sigma_{\text{in}}/\sigma_{\text{ex}}$ between the exterior and the interior solutions, as evaluated by eq 36. The angular frequency ω of the electric fields is rescaled by the threshold amplitude η_{th} defined after eq 35, the conductivity σ_{in} and the dielectric constant ε_{in} of the interior solution.

frequency where the work done by the Maxwell stresses, W_{el} , changes sign, except for prolate/oblate–sphere transitions. In other words, the zeros of W_{el} indicate the morphological transitions predicted by the model. In this section, we analyze the zeros of W_{el} without the limiting frequency regime to study the present model globally.

The general expressions of the work W_{el} done by the Maxwell stresses are given in eq 92 in Appendix B. Because of the complexity of eq 92, here we analyze the morphological transitions assuming that the dielectric constants of the solutions are symmetric across the membrane (i.e., $\varepsilon_w = \varepsilon_{\text{ex}} = \varepsilon_{\text{in}}$). Equation 92 is rewritten in the form of

$$W_{\text{el}} = \frac{6\pi}{5} r_{\text{ex}}^2 s E_0^2 |H|^2 \frac{\sigma_{\text{ex}}^4 \varepsilon_w}{(\sigma_{\text{ex}}^2 + \omega^2 \varepsilon_w^2)(\sigma_{\text{in}}^2 + \omega^2 \varepsilon_w^2)} \Lambda(\bar{\omega}) \quad (37)$$

with

$$\bar{\omega} \equiv \frac{\omega \varepsilon_w}{\sigma_{\text{ex}}} \quad (38)$$

$$H \equiv \frac{1}{(2 + \beta_1)(1 + 2\beta_3) - 2(1 - \beta_1)(1 - \beta_3)} \frac{r_{\text{in}}^3}{r_{\text{ex}}^3} \quad (39)$$

and

$$\Lambda(\bar{\omega}) \equiv A\bar{\omega}^4 + B\bar{\omega}^2 + C \quad (40)$$

A , B , and C are functions of $\chi = \sigma_{\text{in}}/\sigma_{\text{ex}}$, δ , $\varepsilon_{\text{me}}/\varepsilon_w$, and $\sigma_{\text{me}}/\sigma_{\text{ex}}$. The explicit expressions of A , B , and C are given in Appendix C. $\bar{\omega}$ is a rescaled frequency. The polynomial $\Lambda(\bar{\omega})$ is the determinant of the zeros of W_{el} , and the rest of this section is devoted to the analyses of the polynomial $\Lambda(\bar{\omega})$. The number of zeros in W_{el} is determined by the signs of A , B , and C . The dependence of A , B , and C on χ , δ , $\varepsilon_{\text{me}}/\varepsilon_w$, and $\sigma_{\text{me}}/\sigma_{\text{ex}}$ is described in detail in Appendix C. In this section, we outline the properties of A , B , and C for the typical parameters used in the experiments described in section 2 and analyze the zeros of $\Lambda(\bar{\omega})$.

The conductivity of the membrane is negligibly small compared to the conductivities of the exterior and interior solutions, $\sigma_{\text{me}}/\sigma_{\text{ex}} \approx 0$, and the bilayer thickness is orders of magnitudes smaller than the lateral dimension of the vesicle (e.g., $\delta = 1.0 \times 10^{-3}$). In this case, both A and C are positive and very small for all studied values of χ . B changes sign at $\chi \approx 1$. Examples of the frequency dependence of $\Lambda(\bar{\omega})$ for $B > 0$ and $B < 0$ are shown as dashed and solid curves in Figure 5a. For $\chi > 1$, B is positive and there are no zeros in $\Lambda(\bar{\omega})$ as exemplified by the dashed curve in Figure 5a. In other words, the vesicle does not exhibit morphological transitions until the field frequency exceeds the inverse

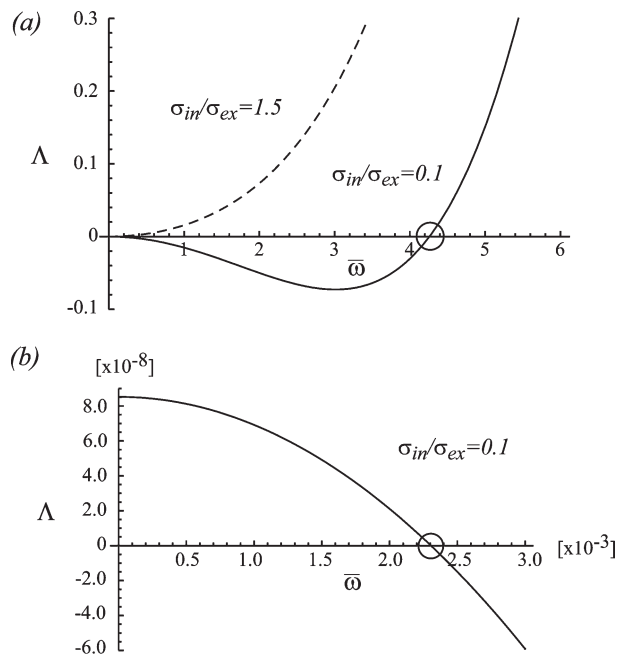


Figure 5. (a) The polynomial $\Lambda(\bar{\omega})$, evaluated by eq 40, is plotted as a function of the rescaled frequency $\bar{\omega}$ for $\sigma_{in}/\sigma_{ex} = 0.1$ as the solid curve and for $\sigma_{in}/\sigma_{ex} = 1.5$ as the broken curve. The zeros of $\Lambda(\bar{\omega})$ indicate morphological transitions and are marked by circles. The angular frequency of the electric field is rescaled by the dielectric constant ϵ_w of water and the exterior conductivity σ_{ex} as $\bar{\omega} \equiv \omega\epsilon_w/\sigma_{ex}$; see eq 38. The dielectric constant ratio ϵ_{me}/ϵ_w between the membrane and water, the ratio r_{in}/r_{ex} between the interior and exterior radius, and the conductivity ratio σ_{me}/σ_{ex} between the membrane and the exterior solutions is fixed to 0.026, 0.999, and 0, respectively. The low-frequency part of the solid curve in (a) is magnified in (b) revealing another zero of $\Lambda(\bar{\omega})$.

Maxwell–Wagner time, at which the prolate–sphere transitions are observed. However, for $\chi < 1$, the sign of B is negative and there are two zeros; see the solid curve in Figure 5a. Figure 5b is the magnification of the solid curve for small $\bar{\omega}$. One zero point is at the $\bar{\omega}$ value on the order of 10^{-3} , and the other is at the $\bar{\omega}$ value on the order of unity. $\bar{\omega}$ is the rescaled frequency defined by eq 38, and ϵ_w/σ_{ex} is on the order of 10^{-6} s for $\sigma_{ex} \approx 1$ mS/m and $\epsilon_w \approx 10^{-9}$ C/V m. Because the sign of the work done by the Maxwell stress changes from positive to negative upon increasing the frequency at the first zero point at $\bar{\omega} \approx 10^{-3}$ (i.e., $\omega \approx 10^{-3}$ Hz), this zero point corresponds to the prolate–oblate transitions that have been observed experimentally; see Figure 1. Interestingly, there is another zero at $\bar{\omega} \approx 1$ (i.e., $\bar{\omega} \approx 10^6$ Hz). Thus, there is a morphological transition from oblate to prolate at the frequency on the order of megahertz upon increasing the frequency, which has not been observed experimentally. This transition is probably hidden by the oblate–sphere transitions, which has been observed at frequencies on the order of megahertz.

In summary, the present theory reproduced all four morphological transitions detected in the experiments and found another morphological transition, which has not been observed experimentally. The latter transition is probably hidden by the oblate–sphere morphological transition, and its presence does not contradict the experimental result. The present theory demonstrates that the work done by the Maxwell stresses is the origin of the prolate–oblate transitions observed in the experiments.

6. Electric Charges Accumulated at the Interfaces

The present model predicts all four types of morphological transitions as observed experimentally for vesicles in ac electric fields. Dielectric physics suggests that electric charges are

accumulated at the interfaces between lossy dielectrics (i.e., at the exterior and interior interfaces of the vesicle), reflecting the relaxation time difference between the two interfacing media.^{30,31} To understand the mechanisms of morphological transitions more intuitively, it is instructive to reinterpret the force densities, represented in eqs 19 and 20, in terms of the electric charges accumulated at the exterior and interior interfaces of the vesicle.

Instead of treating the force densities applied to the exterior and the interior interfaces individually, we consider the net force densities

$$\mathbf{f}_{me}(\theta) = \mathbf{f}_{ex}(\theta) + \mathbf{f}_{in}(\theta)(1 - \delta)^2 \quad (41)$$

applied per unit area of the exterior interface. The area of the interior interface is smaller than the area of the exterior interface because of the finite thickness of the bilayer membrane. The factor $(1 - \delta)^2$ in the second term of eq 41 is the correction for the area difference; see also eq 21. Equation 41 includes higher-order terms with respect to β_1 , β_3 , and δ . To the leading order of the series expansion in powers of β_1 , β_3 , and δ , the net force densities $\mathbf{f}_{me} = (f_{mer}(\theta), f_{me\theta}(\theta), f_{me\phi}(\theta))$ in a spherical coordinate system can be represented as

$$f_{mer}(\theta) = \langle q_{me}(\theta, t) \bar{E}_r(\theta, t) \rangle - \frac{1}{2} \epsilon_w \langle \mathcal{E}_\theta^2(r_{ex}, \theta, t) - \mathcal{E}_\theta^2(r_{in}, \theta, t) \rangle \quad (42)$$

$$f_{me\theta}(\theta) = \langle q_{me}(\theta, t) \mathcal{E}_\theta(r_{in}, \theta, t) \rangle \quad (43)$$

with

$$\bar{E}_r(\theta, t) \equiv \frac{1}{2} (\mathcal{E}_{exr}(r_{ex}, \theta, t) + \mathcal{E}_{inr}(r_{in}, \theta, t)) \quad (44)$$

$$q_{me}(\theta, t) \equiv \epsilon_{ex} \mathcal{E}_{exr}(r_{ex}, \theta, t) - \epsilon_{in} \mathcal{E}_{inr}(r_{in}, \theta, t) \quad (45)$$

and $f_{me\phi}(\theta) = 0$. Because the tangent electric fields $\mathcal{E}_\theta(r, \theta, t)$ are continuous across each interface, the corresponding indices ex, me, and in, are omitted (i.e., $\mathcal{E}(r_{ex}, \theta, t) \equiv \mathcal{E}_{ex\theta}(r_{ex}, \theta, t) = \mathcal{E}_{me\theta}(r_{ex}, \theta, t)$ and $\mathcal{E}_\theta(r_{in}, \theta, t) \equiv \mathcal{E}_{me\theta}(r_{in}, \theta, t) = \mathcal{E}_{in\theta}(r_{in}, \theta, t)$). A brief derivation of eqs 42 and 43 is given in the Supporting Information.

The quantity $q_{me}(\theta, t)$ is the net electric charge density accumulated at the membrane (i.e., the sum of the electric charges accumulated at the exterior and interior interfaces) and is exposed to the effective normal electric field $\bar{E}_r(\theta, t)$. It is important to note that $q_{me}(\theta, t)$ represents true electric charges (e.g., ions in the solutions) and that the electric charges induced by the dielectric polarizations of the membrane and of the solutions do not give rise to the force densities. The first terms in eq 42 and eq 43 represent the force densities arising from the interactions between the net electric charges $q_{me}(\theta, t)$ accumulated at the interfaces and the electric fields $\mathcal{E}_r(\theta, t)$ and $\mathcal{E}_\theta(r_{in}, \theta, t)$. The second term of eq 42 is the net quantity of the so-called electric pressure of Maxwell stresses. Equations 42 and 43 demonstrate that the force densities associated with the Maxwell stresses can be reinterpreted as the force densities arising from the interactions between the electric fields and the accumulated electric charges and those arising from the electric pressure.

It is important to note that this interpretation is possible because of the characteristic geometry of the vesicle, where two solutions of nearly equal dielectric constants are separated by a thin layer of low electric conductivity and low dielectric constant. The accumulated electric charges $q_{me}(\theta, t)$ and the effective normal electric field $\bar{E}_r(\theta, t)$ to which $q_{me}(\theta, t)$ is exposed can be calculated by substituting the expression of electric fields, given by eq 8, into eqs 44 and 45; see section 3.3.

7. Mechanism of Morphological Transition

7.1. Mechanisms of Prolate Deformation in the Low-Frequency Regime. The stable shape of a vesicle in low frequency fields with $|\beta_1| \ll \delta$ and $|\beta_3| \ll \delta$ is provided by a prolate independent of the conductivity ratio χ . Indeed, the amplitude s of the deformation is independent of the conductivities of the interior solutions; see eq 25. The sign of s is determined by the compressive Maxwell stresses arising from the tangent electric fields; see the second term on the right-hand side of eq 17. In section 6, these Maxwell stresses are represented as an electric pressure; see the second term on the right-hand side of eq 42. Because lipid membranes are electrical insulators, both the conduction currents and the displacement currents across the membranes are negligibly small in the low-frequency regime. The electric fields are distributed to avoid the membrane because of its high electrical resistivity against both conductive and displacement currents and become tangent to the surface of the vesicle. Because of the geometry of the vesicle, the magnitudes of the tangent electric fields are largest at the equator; see Figure 2. The tangent electric fields generate the compressive Maxwell stresses and push the equator of the vesicle from the exterior to deform it into a prolate. The membrane completely insulates the interior solution from the electric field, and the conductivity of the interior solution does not affect the electric field distributions and the Maxwell stresses in the low-frequency regime. Thus, the amplitude s of deformation is independent of the conductivities of the interior solutions (eq 25), which are independent of β_3 .

7.2. Mechanisms of the Prolate–Oblate Morphological Transition. In the intermediate frequency regime, the vesicle exhibits morphological transitions from prolate to oblate for $\chi < 1$ whereas it keeps its prolate morphology for $\chi > 1$ with increasing field frequency. The conduction current flowing across the membrane is still negligibly small. However, the displacement currents flowing across the membrane increase with the frequency and are not negligible in the frequency regime of interest. Because the displacement currents can possibly flow across the membrane, the electric fields, which were tangential to the membrane in the low-frequency regime, now attain a normal component as well. The electric fields penetrate into the interior solution, and the conductivity of the interior solution affects the distribution of the electric fields as well as the Maxwell stresses. In the intermediate regime, both the tensile and the compressive contributions to the Maxwell stresses as well as the shear Maxwell stresses are not negligible but generate force densities in the r and θ directions to deform the vesicle.

The Maxwell stresses have tensile and compressive contributions arising from the normal and tangent electric fields, respectively; see eq 17. In the reinterpretation of section 6, the tensile Maxwell stresses arising from the normal electric fields generate the force densities that can be rewritten in the form of the interactions between accumulated electric charges and the normal electric fields; see the first term on the right-hand side of eq 42. Furthermore, the compressive Maxwell stresses arising from the tangent electric fields generate force densities that can be rewritten as an electric pressure; see the second term on the right-hand side of eq 42. Because the tensile and compressive contributions to the Maxwell stresses are interpreted differently, it is important to discuss these two contributions separately.

First, we discuss the force densities arising from the interactions between accumulated electric charges and the electric fields (i.e., the shear Maxwell stresses and the tensile Maxwell stresses arising from the normal electric fields). Following the argument in

section 6, we consider the net force densities of the membrane instead of individual force densities applied to the exterior and interior interfaces. The net charge density $q_{\text{me}}(\theta, t)$ accumulated at the membrane is represented by eq 45, where $\mathcal{E}_{\text{ex}}(r_{\text{ex}}, \theta, t)$ and $\mathcal{E}_{\text{in}}(r_{\text{in}}, \theta, t)$ are given by eq 8. In the intermediate frequency regime, $|\beta_1|$, $|\beta_3|$, and δ are of the same order of magnitudes and are orders of magnitudes smaller than 1; see section 4. The asymptotic expression of the net electric charge density $q_{\text{me}}(\theta, t)$ accumulated at the membrane for this regime is derived as

$$q_{\text{me}}(\theta, t) = \frac{3}{2\delta} E_0 \cos \theta \left[\frac{\epsilon_{\text{ex}}}{\sigma_{\text{ex}}} - \frac{\epsilon_{\text{in}}}{\sigma_{\text{in}}} \right] \frac{\omega \epsilon_{\text{me}}}{\sqrt{1 + \frac{\omega^2}{\omega_0^2}}} \cos(\omega t + \phi_0) \quad (46)$$

with

$$\tan \phi_0 = \frac{\omega_0}{\omega} \quad (47)$$

by expanding eq 45 with respect to β_1 , β_3 , and δ and by using eqs 62 and 63. The polarity of the net electric charge density accumulated at the membrane depends on the difference in the relaxation time of the exterior and interior solutions; see the contents of the square brackets in eq 46. Because we have assumed that the dielectric constants of the solutions are not sensitive to the solute concentrations (i.e., $\epsilon_{\text{ex}} = \epsilon_{\text{in}} = \epsilon_{\text{w}}$), the polarity of the electric charge densities changes sign at $\chi = 1$. The asymptotic expression of the normal and the tangent electric fields, which are exposed to the accumulated electric charges $q_{\text{me}}(\theta, t)$, are calculated by eqs 8 and 44 for $\mathcal{E}_{\theta}(r_{\text{in}}, \theta, t)$ in terms of β_1 , β_3 , and δ and are written as

$$\bar{E}_r(\theta, t) \approx \frac{3}{4\delta} E_0 \cos \theta \left[\frac{1}{\sigma_{\text{ex}}} + \frac{1}{\sigma_{\text{in}}} \right] \frac{\omega \epsilon_{\text{me}}}{\sqrt{1 + \frac{\omega^2}{\omega_0^2}}} \cos(\omega t + \phi_0) \quad (48)$$

$$\mathcal{E}_{\theta}(\theta, t) \approx -\frac{3}{2\delta} E_0 \sin \theta \frac{\omega \epsilon_{\text{me}}}{\sigma_{\text{in}}} \frac{1}{\sqrt{1 + \frac{\omega^2}{\omega_0^2}}} \cos(\omega t + \phi_0) \quad (49)$$

by the lowest-order term. Note that the tangent electric fields $\mathcal{E}_{\theta}(\theta, t)$ are uniform across the two interfaces and the membrane in the asymptotic limit (i.e., $\mathcal{E}_{\theta}(r_{\text{ex}}, \theta, t) \approx \mathcal{E}_{\theta}(r_{\text{in}}, \theta, t)$) and are denoted as $\mathcal{E}_{\theta}(\theta, t)$ by omitting r_{ex} and r_{in} . It is important to note that the phases of the oscillation of the electric fields for both the normal and the tangent components match the phase of the oscillation of the electric charges accumulated at the interfaces of the vesicle.

Snapshots of the accumulated electric charges $q_{\text{me}}(\theta, t)$ and the electric fields $\bar{E}_r(\theta, t)$ and $\mathcal{E}_{\theta}(\theta, t)$ are displayed in Figure 6 according to eqs 46, 48, and 49 by taking into account the phase matching. The force densities exerted on the vesicle are given by the product of the accumulated electric charges $q_{\text{me}}(\theta, t)$ and the electric fields, $\bar{E}_r(\theta, t)$ and $\mathcal{E}_{\theta}(\theta, t)$; see eqs 42 and 43. When the electric fields reverse the direction, the polarities of the accumulated electric charges reverse synchronously to keep the directions of the force densities constant because of phase matching. For $\chi > 1$, the accumulated electric charges experience tangential force densities of $f_{\text{me}\theta}(\theta, t)$ that point toward the poles. The tensile Maxwell stresses arising from the normal electric fields generate normal force densities $f_{\text{mer}}(\theta, t)$ at the poles toward the exterior of the vesicle. The tangent and the normal force densities do not compete but both deform the vesicle into a prolate shape as illustrated in Figure 6a. For $\chi < 1$, however, the accumulated electric charges experience the tangential forces $f_{\theta}(t)$ toward the equator. The tensile Maxwell stresses arising from the normal electric fields lead to normal force

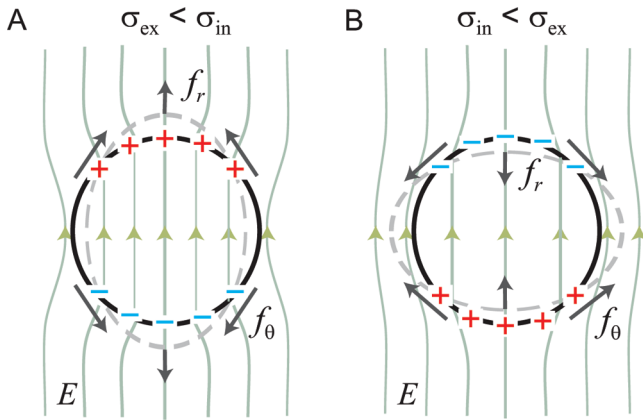


Figure 6. Snapshots of the distributions of the electric charges accumulated by the Maxwell–Wagner mechanism and the force densities arising from the interactions between the electric fields and the accumulated charges for (A) $\sigma_{\text{ex}} < \sigma_{\text{in}}$ and (B) $\sigma_{\text{in}} < \sigma_{\text{ex}}$. The sum of the electric charges accumulated at the exterior and the interior interfaces (i.e., $q_{\text{mc}}(\theta, t)$) is depicted; see section 6. \mathbf{f}_r and \mathbf{f}_θ are the net normal and tangent force densities, respectively. During half of the time, the ac electric fields are directed opposite to the electric fields depicted in the Figures. Since the accumulated electric charges reverse their polarity in phase with the reversal of the electric fields, the force densities are always directed in the same direction for any period of time.

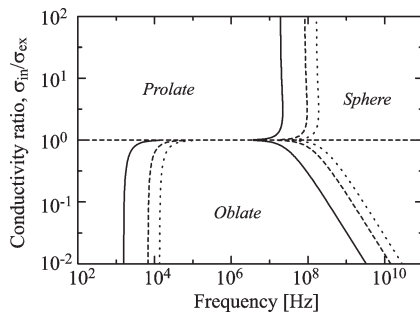


Figure 7. Morphological diagram predicted theoretically as a function of conductivity ratio $\sigma_{\text{in}}/\sigma_{\text{ex}}$ between the interior and exterior solutions and frequency ν , $\nu = \omega/2\pi$. Equations 31 and 34 are used to plot the diagram. The solid curve, the broken curve, and the dotted curve are calculated for $\sigma_{\text{in}} = 1.5, 6.5$, and $13 \mu\text{S/m}$, respectively. For the calculation, the membrane thickness l_{mc} and the radius of the vesicle r_{mc} are taken to be 4 nm and $20 \mu\text{m}$. The dielectric constants of the membrane ϵ_{mc} and the water ϵ_{w} are $2\epsilon_0$ and $80\epsilon_0$. The rescaled threshold amplitude η_{th} of deformation (eq 35) is 0.59 . This threshold value corresponds to a deformation amplitude of $s = 0.5 \mu\text{m}$ for a vesicle with a bending rigidity of $\kappa = 2.0 \times 10^{-19} \text{ J}$ in an electric field with a magnitude of 200 V/cm .

densities $f_r(\theta, t)$ at the poles toward the interior of the vesicle for $\chi < 1$. The tangent and normal force densities do not compete but both deform the vesicle into an oblate shape.

The prolate deformation in the low-frequency regime is ascribed to the electric pressure (i.e., the compressive Maxwell stresses arising from the tangential electric fields). With increasing frequency, the electric fields around the vesicle are redirected in the membrane normal because of the displacement currents across the membrane and electric charges are accumulated at the interfaces of the vesicle. For conductivity conditions with $\chi > 1$, the force densities arising from the interactions between the accumulated electric charges and the electric fields are applied in the direction to deform the vesicle further into a prolate. However, for conductivity conditions with $\chi < 1$, the latter force densities act to deform the vesicle into an

oblate with increasing field frequency and compete with the electric pressure. The vesicle exhibits the prolate–oblate morphological transition (i.e., transition 4 in Figure 1) when the force densities arising from the interactions between the electric fields and the accumulated electric charges win over the electric pressure. The polarities of the electric charges accumulated at the interfaces of the vesicle change sign at $\chi = 1$ by changing the conductivity condition; see the inside of the square brackets in eq 46 and Figure 6. It reverses the direction of the force densities arising from the interactions between the accumulated charges and the electric fields. The vesicle exhibits another type of prolate–oblate morphological transition (i.e., transition 3 at $\chi = 1$ in Figure 1) by changing the conductivity ratio χ while keeping the field frequency in the intermediate frequency regime. In short, the prolate–oblate transition originates from the competition between the electric pressure and the force densities arising from the interactions between the accumulated charges and the electric fields or the reversing of the polarity of the accumulated electric charges at $\chi = 1$.

7.3. Contributions of the Vesicle Geometry to the Prolate–Oblate Frequency Transition. One important physical concept involved in the prolate–oblate transition is the redirections of the electric fields at the interfaces by the displacement currents. The vesicles are essentially insulators, and the conduction currents across the membrane are negligible. The displacement currents across the membrane increase with the field frequency, and the electric fields are redirected to some extent towards the membrane normal to allow the displacement currents to flow. The geometries of the vesicles, which are characterized by $\delta \equiv l_{\text{mc}}/r_{\text{ex}}$, also are involved in the redirection of the electric fields. For spherical vesicles (i.e., $\delta \neq 0$), the electric fields can be directed along the tangent of the vesicles to avoid currents flowing across the membranes when the frequency of the electric fields is sufficiently low. It is necessary to increase the field frequency to redirect the electric fields towards the normal of the membrane surface. However, when the external electric fields are applied perpendicular to a slab of membrane (i.e., $\delta \rightarrow 0$), the electric fields cannot avoid the membrane even in low-frequency electric fields because of the geometry of the system. In this case, the frequencies of the prolate–oblate transitions converge to $\omega_c \rightarrow 0$ (eq 31) because the electric fields penetrate into the internal solutions even without increasing the displacement currents owing to the geometry. Therefore, the frequencies of the prolate–oblate transitions are determined by the competition between the geometric parameter δ and the field frequency ω . This is the reason that the three frequency regimes are divided on the basis of the comparison between the magnitudes of δ , $|\beta_1|$, and $|\beta_3|$. The frequencies of prolate–oblate transitions are dependent not only on the interior conductivities σ_{in} but also on the geometries δ (i.e., the size of the vesicles) in the morphological diagram; see eq 31. The shifts of the transition frequency for different interior conductivities are partially seen in Figure 1. However, systematic experiments, which focus on the dependence of the transition frequencies on the size of the vesicles and the interior conductivities, are necessary to check the validity of the present theory.

7.4. Mechanisms of Prolate/Oblate–Sphere Morphological Transitions. The prolate/oblate–sphere transitions originate from the decay of the work done by the Maxwell stress in the high-frequency regime; see section 4.3. Though the prolate–sphere and oblate–sphere transitions (i.e., transitions 1 and 2) were denoted as separate transitions in the experiment in section 2, the origins of the two morphological transitions are common. In the high-frequency regime, in which prolate/oblate–sphere transitions were observed experimentally, $|\beta_1|$ and $|\beta_3|$ are orders

of magnitude larger than δ ; see section 4. The asymptotic expression of the net electric charges $q_{\text{me}}(\theta, t)$ accumulated at the membrane for this regime are calculated as

$$q_{\text{me}}(\theta, t) = 3E_0 \cos \theta \frac{\sigma_{\text{ex}} \sigma_{\text{in}}}{2\sigma_{\text{ex}} + \sigma_{\text{in}}} \left[\frac{\epsilon_{\text{ex}}}{\sigma_{\text{ex}}} - \frac{\epsilon_{\text{in}}}{\sigma_{\text{in}}} \right] \frac{1}{\sqrt{1 + \frac{\omega^2}{\omega_s^2}}} \cos(\omega t + \phi_s) \quad (50)$$

with

$$\tan \phi_s = -\frac{\omega}{\omega_s} \quad (51)$$

by expanding eq 45 with respect to δ/β_1 and δ/β_3 by the lowest-order terms. The accumulated electric charge densities $q_{\text{me}}(\theta, t)$ decay gradually with frequency in the asymptotic limit. The inverse Maxwell–Wagner charging time ω_s provides the cutoff frequencies for the electric charge decay; see eq 34. The electric charges, which play a role in the conduction currents, cannot follow electric fields of frequency larger than ω_s . In the intermediate- and high-frequency regimes, the force densities arising from the interactions between the electric fields and the accumulated electric charges are responsible for vesicle deformations to prolate or oblate. Because those force densities are proportional to the net accumulated electric charges (eq 45), the vesicle gradually returns to a sphere by increasing the frequency.

At frequency higher than the inverse Maxwell–Wagner time ω_s , the displacement currents dominate the conduction currents in the exterior and interior solutions as well as in the membrane. The displacement currents induce electric charges at the two interfaces of the vesicle by generating dielectric polarization in the three media. However, the force densities are not generated by the electric charges induced by the dielectric polarizations but by the true electric charges accumulated by the conduction currents; see section 6. The net true electric charge densities are accumulated at the membrane by the difference between the electric fluxes coming into the membrane and those going out of the membrane; see eq 45. The discontinuity of the electric flux across the membrane decreases with frequency because the electric fields are distributed according to the dielectric constants rather than the conductivities in the high-frequency region; see eq 12. Therefore, the redistribution of the electric fields by increasing the frequency is the origin of the decay of the accumulated electric charges and of the prolate/oblate–sphere morphological transitions.

One may wonder whether the compressive Maxwell stresses arising from the tangent electric fields (i.e., the electric pressure represented by eqs 42) can contribute to the deformation of the vesicle in the high-frequency regime after the force densities arising from the interactions between the accumulated electric charges and the electric fields decay. In the low-frequency regime, the tangent electric fields are generated only at the exterior of the vesicle because the membrane insulates the electric fields and the tangent electric fields generate Maxwell stresses to push the equator of the vesicle into a prolate from the exterior. However, in the high-frequency regime, the tangent electric fields are continuous across the membranes and the Maxwell stresses arising from the tangent electric fields push the equator of the vesicle not only from the exterior but also from the interior within the same order of magnitude. As a result, the Maxwell stresses applied at the exterior and interior interfaces cancel each other (eq 42) and the Maxwell stresses arising from the tangent electric fields are no longer included in the leading terms of the deformations in the high-frequency regime.

8. Discussion

8.1. Electric Fields in the Low-Frequency Regime. It is instructive to examine the electric fields around the vesicle for low frequencies. In the latter frequency regime, $|\beta_1|$ and $|\beta_3|$ are much smaller than δ ; see section 4. The asymptotic expression of normal field components for this regime is derived by expanding eq 8 for $k = 2$ with respect to β_1/δ and β_3/δ as

$$\mathcal{E}_{\text{mer}}(r_{\text{ex}}, \theta, t) = \frac{3}{2\delta} E_0 \cos \theta \cos \omega t \quad (52)$$

by the lowest-order terms. The normal electric fields are uniform in the membrane (i.e., $\mathcal{E}_{\text{mer}}(r_{\text{ex}}, \theta, t) \simeq \mathcal{E}(r_{\text{in}}, \theta, t)$) by the lowest-order terms. In a similar manner, the asymptotic forms of the normal electric fields at the solution sides of the exterior and interior interfaces can be written as

$$\mathcal{E}_{\text{exr}}(r_{\text{ex}}, \theta, t) = -\frac{3}{2\delta} \frac{\omega \epsilon_{\text{me}}}{\sigma_{\text{ex}}} E_0 \cos \theta \sin \omega t \quad (53)$$

$$\mathcal{E}_{\text{inr}}(r_{\text{in}}, \theta, t) = -\frac{3}{2\delta} \frac{\omega \epsilon_{\text{me}}}{\sigma_{\text{in}}} E_0 \cos \theta \sin \omega t \quad (54)$$

respectively, which are obtained by expanding eq 8 for $k = 1$ and 3 with respect to β_1/δ and β_3/δ by the lowest-order terms. For typical experimental parameters, the magnitudes of the normal electric fields in the membrane are on the order of 10^6 V/cm whereas the magnitudes of the normal electric fields on the solution sides of the interfaces are on the order of 2 V/cm (e.g., $\delta = 10^{-4}$, $E_0 = 100$ V/cm, $\sigma_{\text{ex}} = \sigma_{\text{in}} = 10^{-3}$ S/m, $\epsilon_{\text{me}} = 2\epsilon_0$, and $\omega = 10^2$ Hz). This estimate suggests that the magnitudes of the electric fields change abruptly, by a factor of 10^6 , across the exterior and interior interfaces. One may wonder whether the large jumps in the normal electric fields across the interfaces are physical.

In the low-frequency regime, the conduction currents, which are proportional to the conductivities, are responsible for the electric currents flowing through the exterior and interior solutions whereas the displacement currents, which are proportional to the susceptibility $\omega \epsilon_{\text{me}}$, are responsible for the electric currents across the membrane because of its extremely low conductivity. The conductivities of the solutions are orders of magnitudes larger than the susceptibility, $\omega \epsilon_{\text{me}}$, of the membrane. Thus, the solutions behave as almost perfect conductors and the membrane behaves as a perfect insulator. Because the electric fields in the conductive solutions are relatively small, the electric voltage between the two electrodes in the chamber is essentially applied across the membranes whose thickness is on the order of a nanometer. Thus, the large difference in the ability of both types of currents to flow between the membrane and the solutions and the nanoscopic thickness of the membrane lead to the large differences in the magnitudes of the electric fields between the membrane and the solutions.

Because our theory is based on macroscopic electrodynamics, we assumed that the electric charges were accumulated at the interfaces but ignored the finite thickness of the accumulated layer; see section 6. The abrupt changes in the electric fields reflect this simplifying assumption. At the molecular level, the ions form diffuse layers in the vicinity of the membrane surfaces. The diffuse layers may be described by spatially dependent (effective) dielectric constants and were studied extensively in the context of induced charge electroosmosis (ICEO).^{34,35} The thicknesses of the diffuse layer at the exterior and interior interfaces are estimated by the molecular field

(34) Murtsovkin, V. A. *Colloid J.* **1996**, *58*, 341.

(35) Lacoste, D.; Menon, G. I.; Bazant, M. Z.; Joanny, J. F. *Eur. Phys. J. E* **2009**, *28*, 243–264.

theory to be $(D\epsilon_{\text{ex}}/\sigma_{\text{ex}})^{1/2}$ and $(D\epsilon_{\text{in}}/\sigma_{\text{in}})^{1/2}$, respectively, where D is the diffusion constant and is on the order of 10^{-5} cm²/s for small ions such as sodium and chloride. For typical experimental parameters, the thickness of the diffuse layer is on the order of 27 nm for $\sigma_{\text{ex}} = \sigma_{\text{in}} = 10^{-3}$ S/m and $\epsilon_{\text{ex}} = \epsilon_{\text{in}} = 80\epsilon_0$. Therefore, the amplitudes of the normal electric fields do not change discontinuously but smoothly across the diffuse layer, whose thickness is on the order of 27 nm. Because the thickness of the diffuse layer is much smaller than the radius of the vesicle, the electric fields and the force densities calculated in the present study are sufficiently accurate to provide a reliable description of the morphological transitions.

Molecular field theory assumes a continuous distribution of ions around the membrane surfaces. The discrete nature of the ions may affect the gradient of the electric fields as discussed in ref 36, but these discrete ion effects are beyond the scope of our study.

Experimentally, strong electric fields open pores in membranes.^{10,29,37} In the low-frequency regime, the present theory estimates the transmembrane potentials to be ~ 0.6 V for our experimental geometry whereas the transmembrane potentials necessary to induce electroporation are ~ 0.1 – 1 V.³⁷ Here, the transmembrane potential was estimated by eq 52 for $E_0 = 200$ V/cm and $r_{\text{ex}} = 20$ μm . Thus, one might worry about the strong electric fields opening pores in the membrane and the effect of these pores on the experimentally determined morphological diagram as displayed in Figure 1. However, no electroporation of the vesicles was detected in the experiments described in section 2.

8.2. Comparison with the Electrohydrodynamic Model.

Previously, the prolate–oblate transitions for $\chi < 1$ were predicted numerically by an electrohydrodynamic model.²⁵ In this theory, the membrane was modeled as a capacitor with effective transmembrane potentials based on classical studies by Schwan.²⁷ Vlahovska et al.²⁵ estimated the frequencies for the prolate–oblate transitions from the charging time of the membrane capacitance. The focus of the electrohydrodynamic theory was on possible hydrodynamic flows driven by ac electric fields, and the electrostatics underlying the prolate–oblate transitions were not analyzed in detail. In contrast, the present study emphasizes the physical mechanisms underlying the prolate–oblate transitions; see sections 7.2 and 7.3. Furthermore, we derived analytical expressions for the frequencies of the prolate–oblate transitions, and these frequencies are accessible experimentally; see section 8.3.

In the electrohydrodynamic theory, the frequencies of the prolate/oblate–sphere transitions were estimated by inverse Maxwell–Wagner time. This theory, however, employs effective transmembrane potentials²⁷ in which Maxwell–Wagner relaxation is not taken into account, though this relaxation is the physical mechanism underlying the prolate/oblate–sphere transitions. In contrast, these relaxation mechanisms are naturally included by solving the Maxwell equations for the quasistatic approximation. The theory presented here provides a unified description of all experimentally observed morphological transitions of the vesicle in ac electric fields.

8.3. Comparison with Experiment. The morphological diagrams predicted in the present theory are qualitatively in agreement with the experimentally determined morphological diagrams. However, there remain some quantitative discrepancies. For comparison, the morphological diagram of a vesicle with a 20 μm radius is calculated for typical experimental parameters using eqs 31 and 36, and the results are shown in Figure 7.

The present theory predicts the frequency at which the vesicle exhibits the prolate–oblate transition (transition 4 in Figure 1), roughly in agreement with experiments. However, the frequencies

of these prolate–oblate transitions depend not only on the conductivity ratio χ and on the absolute value of σ_{in} but also on the radius of the vesicle; see eq 31. Antonova et al.³⁸ and Peterlin³⁹ found that the frequency for prolate–oblate transitions is inversely proportional to the radius of the vesicle. In our present theory, the frequency for prolate–oblate transitions is given by eq 31 with the parameter δ defined in eq 23. Thus, the present theory is in agreement with those experimental results. However, in these latter experiments, the vesicles were prepared under symmetric conductivity conditions, which are sensitive to impurities, in the experiments in refs 38 and 39. The prolate–oblate transitions were probably induced by ion impurities as suggested by the authors.^{38,39} More systematic experiments are necessary for a quantitative comparison between theory and experiment. Equation 31 derived here predicts the reduced frequency $r_{\text{me}}\omega_c/\sigma_{\text{in}}$ for the prolate–oblate transitions as a function of χ collapse onto one curve regardless of the vesicle size and the conductivity of the vesicle interior. This prediction is accessible via experiments.

The frequencies of prolate/oblate–sphere transitions (transitions 1 and 2 in Figure 1) are not directly dependent on the size of the vesicle; see eq 36. Though the shape of the boundary between prolate/oblate and sphere in the theoretically predicted morphological diagram agrees well with the experiments, the frequencies of these transitions are predicted to be much higher than the experimentally determined values. The frequencies of prolate/oblate–sphere transitions are proportional to σ_{in} (eq 36), and the transition frequencies shift steadily to the higher frequency with σ_{in} . However, the experimentally determined shifts in the transition frequencies with σ_{in} are not as large as the theoretically predicted shifts; see Figures 1 and 7. In spite of this quantitative discrepancy, the present theory predicted the shape of the boundaries between the prolate/oblate and sphere quite well. Thus, one might speculate that another physical mechanism, which changes the conductivities and/or the dielectric constants of the solutions to effective values, might be involved.

In the present model, we assumed that the conductivities and dielectric constants of the aqueous solutions are homogeneous and frequency-independent. However, the following factors may influence these parameters. First, the diffuse layers induced by lipid–ion electrostatic interactions may affect the local conductivities and dielectric constants in the immediate vicinity of the membrane.^{40–42} Second, the bulk solution conductivities may exhibit dispersion at high frequencies. Third, the different mobilities of the positive and negative charges can change the effective dielectric constants in the membrane and the diffuse layers; see also section 8.1. These space and frequency dependencies of the conductivities and the dielectric constants are sensitive to the ion species; experiments in this direction may clarify the origin of the difference between the theoretically predicted and experimentally measured transition frequencies.

9. Conclusions

The deformations of the vesicles in ac electric fields were studied theoretically and experimentally for a wide range of field frequency and conductivity conditions. The comparison of theory and experiment indicates that the conduction and displacement currents flowing through the system provide the basic mechanisms for the morphological transitions of vesicles in ac electric fields because the vesicle shapes are sensitive to the conductivity ratio χ and the frequency. The origins and mechanisms of the morphological transitions were studied by extending the Winterhalter–Helfrich model to asymmetric conductivity conditions across the

(36) Nelson, A. P.; McQuarrie, D. A. *J. Theor. Biol.* **1975**, *55*, 13–27.

(37) Harbich, W.; Helfrich, W. *Z. Naturforsch.* **1979**, *34*, 1063–1065.

(38) Antonova, K.; Vitkova, V.; Mitov, M. D. *Eur. Phys. Letts.* **2010**, *89*, 38004.

(39) Peterlin, P. *J. Biol. Phys.* **2010**, DOI:10.1007/s10867-010-9187-3.

membrane and to a wide range of frequencies. The free energies were constructed as the sum of the bending energies of the membrane and the work done by the Maxwell stresses. The stable shapes of the vesicle were determined by the conditions used to minimize the free energies. The morphological diagram predicted in the present theory is qualitatively in agreement with that determined experimentally.

The true electric charges are accumulated at the two interfaces of the vesicle by the so-called Maxwell–Wagner mechanism.^{30,31} The mechanisms of the four morphological transitions are elucidated on the basis of the electric pressure of the Maxwell stresses and the electric forces arising from the interactions between the electric fields and the accumulated electric charges. The electric pressure deforms the vesicle to a prolate in the low-frequency regime. The accumulated electric charges increase with frequency because the displacement currents across the membrane redirect the electric fields near the interfaces toward the membrane normal. For smaller interior conductivities or $\chi < 1$, the vesicle exhibits prolate–oblate transitions (i.e., transitions 2 and 3 in Figure 1) when the electric forces arising from the interactions between accumulated electric charges and the electric fields overcome the electric pressure. For larger interior conductivities or $\chi > 1$, electric charges of opposite polarities are accumulated at the vesicle, and the electric forces arising from the interactions between accumulated electric charges and the electric fields, together with the electric pressure, deform the vesicle into a prolate. Figure 6 describes the basic mechanism underlying the prolate–oblate transitions. The prolate–sphere and oblate–sphere transitions, which were observed in the high-frequency regime for both $\chi > 1$ and $\chi < 1$, were ascribed to the decay of the accumulated true electric charges. Therefore, we conclude that the true electric charges accumulated at the vesicle interfaces play an essential role in the morphological transitions of vesicles in ac electric fields.

In the present study, we carefully examined the electric fields around the vesicle with spherical shell geometry. Though further effort is necessary to reach quantitative agreement with experiments, the present study is an important step in understanding the electro-deformation of vesicles in ac electric fields. The equation of the deformation amplitudes represented as a function of the magnitude and the frequency of the applied ac electric fields should be useful in extracting information on the mechanical properties of vesicles in electro-deformation experiments.^{13,29,43} Vesicles can assume spherocylindrical shapes (e.g., tubelike and disklike morphologies) when exposed to dc pulses. Those shapes are transient and observable only for a short time period. The overall aspect ratio of the shapes depends on the conductivity ratio between the vesicle interior and exterior in a manner that is analogous to the deformation of vesicles in ac electric fields.¹⁰ Therefore, it is of interest to extend the present theory to the transient shapes of the vesicles in dc pulses. Furthermore, we believe that the present study provides a basis to understand other electric phenomena observed for vesicles, such as electroporation (electropermeabilization),^{10,29,37} liposome electroformation,^{11,12} and electrohydrodynamics.^{29,44}

After the completion of this work, we became aware of a recent study by Peterlin reporting an extension of the Winterhalter–Helfrich calculations to asymmetric conductivity conditions.³⁹ In the latter work, the morphological diagram was calculated numerically but the physical mechanisms underlying the morphological transitions were not analyzed in detail.

Acknowledgment. We thank Margarita Staykova (Princeton) and Petia Vlahovska (Dartmouth College) for fruitful discussions.

Appendix A: Explicit Expressions for Electric Fields

In the quasistatic approximation, it is possible to define the electric potentials $U_k(r, \theta)$ that satisfy the Laplace equations $\nabla^2 U_k(r, \theta) = 0$ for each medium; see Supporting Information. The electric fields $\mathbf{E}_k(r, \theta)$ for $k = 1, 2$, and 3 are derived from the electric potentials $U_k(r, \theta)$ of the corresponding medium as $\mathbf{E}_k(r, \theta) = -\nabla U_k(r, \theta)$. The Laplace equations have solutions that approach eq 7 far away from the vesicle and satisfy eqs 11 and 12 at the exterior and interior interfaces. The latter solutions have the form³²

$$U_k(r, \theta) = -E_k^c r \cos \theta + \frac{\mu_k \cos \theta}{r^2} \quad (55)$$

with $k = 1, 2$, and 3. Note that the first and second terms have the form of the electric potentials arising from constant electric fields in the z direction and that arising from the image dipoles located at the center of the vesicle, respectively. The amplitudes E_k^c and μ_k for $k = 1, 2$, and 3 are determined to satisfy eqs 11 and 12 at the exterior and interior interfaces of the vesicle and approach uniform applied electric fields (eq 7) far away from the vesicle, $r \rightarrow \infty$. μ_3 is zero because the electric potentials and electric fields do not diverge at the center of the vesicle, $r = 0$. The amplitudes E_k^c and μ_k for $k = 1, 2$, and 3, determined by such boundary conditions, are derived as

$$E_1^c = E_0 \quad (56)$$

$$E_2^c = \frac{3(1+2\beta_3)}{(2+\beta_1)(1+2\beta_3)-2(1-\beta_1)(1-\beta_3)\frac{r_{in}^3}{r_{ex}^3}} E_0 \quad (57)$$

$$E_3^c = \frac{9\beta_3}{(2+\beta_1)(1+2\beta_3)-2(1-\beta_1)(1-\beta_3)\frac{r_{in}^3}{r_{ex}^3}} E_0 \quad (58)$$

$$\mu_1 = r_{ex}^3 E_0 - \frac{3 \left[(1+2\beta_3) - (1-\beta_3) \frac{r_{in}^3}{r_{ex}^3} \right]}{(2+\beta_1)(1+2\beta_3)-2(1-\beta_1)(1-\beta_3)\frac{r_{in}^3}{r_{ex}^3}} r_{ex}^3 E_0 \quad (59)$$

$$\mu_2 = \frac{3(1-\beta_3)r_{in}^3}{(2+\beta_1)(1+2\beta_3)-2(1-\beta_1)(1-\beta_3)\frac{r_{in}^3}{r_{ex}^3}} E_0 \quad (60)$$

$$\mu_3 = 0 \quad (61)$$

with

$$\beta_1 \equiv \frac{\sigma_2 - i\omega\epsilon_2}{\sigma_1 - i\omega\epsilon_1} \quad (62)$$

$$\beta_3 \equiv \frac{\sigma_2 - i\omega\epsilon_2}{\sigma_3 - i\omega\epsilon_3} \quad (63)$$

The parameters β_1 and β_3 represent the ratio between the membrane admittance, ψ_{me} , and the admittances of the exterior and interior solutions, ψ_{ex} and ψ_{in} , respectively. r_{in} and r_{ex} are the interior and the exterior radii of the vesicle. In the symmetric conductivity condition across the membrane (i.e., $\beta_1 = \beta_3$),

(40) Bockmann, R. A.; Grubmüller, H. *Angew. Chem., Int. Ed.* **2004**, *43*, 1021–1024.

(41) Clarke, R. J.; Lupfert, C. *Biophys. J.* **1999**, *76*, 2614–2624.

(42) Klasczyk, B.; Lipowsky, R.; Dimova, R. To be submitted for publication.

(43) Gracià, R. S.; Bezlyepkina, N.; Knorr, R. L.; Lipowsky, R.; Dimova, R. *Soft Matter* in press, DOI:10.1039/B920629A.

(44) Staykova, M.; Lipowsky, R.; Dimova, R. *Soft Matter* **2008**, *4*, 2168–2171.

eqs 57–61 return to the equations derived by Winterhalter and Helfrich.¹⁴

Appendix B: Derivation of the Work Done by the Maxwell Stresses

The derivation of W_{el} of lowest order in s is summarized in this section. W_{el} is the work done by the Maxwell stresses, and first we derive the components of the Maxwell stress tensor. To calculate the Maxwell stresses, it is necessary to know the electric field distributions in the vicinity of the exterior and interior vesicle interfaces. The electric field distributions in the vicinity of a spherical vesicle are derived in eq 8. Because of $s \ll r_{me}$, it is sufficient to calculate the electric field distributions for a spherical vesicle. The r component of the electric fields at the exterior interface is represented as

$$\mathcal{E}_{kr}(r_{ex}, \theta, t) = \frac{1}{2} [\alpha_{k,ex} e^{-i\omega t} + \alpha_{k,ex}^* e^{i\omega t}] E_0 \cos \theta \quad (64)$$

for $k = 1$ and 2 , where subscripts 1 and 2 indicate the electric fields on the exterior solution side and membrane side of the exterior interface. Subscript “ex” in $\alpha_{1,ex}$ and $\alpha_{2,ex}$ indicate the exterior interface. We do not use subscripts “ex” and “in” to indicate the exterior and interior solutions and use 1 and 3 in this section to avoid confusion. $\alpha_{1,ex}$ and $\alpha_{2,ex}$ are written as

$$\alpha_{1,ex} = \frac{3\beta_1 \left[(1+2\beta_3) + 2(1-\beta_3) \frac{r_{in}^3}{r_{ex}^3} \right]}{(2+\beta_1)(1+2\beta_3) - 2(1-\beta_1)(1-\beta_3) \frac{r_{in}^3}{r_{ex}^3}} \quad (65)$$

$$\alpha_{2,ex} = \frac{3 \left[(1+2\beta_3) + 2(1-\beta_3) \frac{r_{in}^3}{r_{ex}^3} \right]}{(2+\beta_1)(1+2\beta_3) - 2(1-\beta_1)(1-\beta_3) \frac{r_{in}^3}{r_{ex}^3}} \quad (66)$$

Because of one of the boundary conditions (eq 11), the θ component of the electric fields is continuous across the interfaces. The θ component of the electric fields at the exterior interface is written as

$$\mathcal{E}_{\theta}(r_{ex}, \theta, t) = \frac{1}{2} [\gamma_{ex} e^{-i\omega t} + \gamma_{ex}^* e^{i\omega t}] E_0 \sin \theta \quad (67)$$

with

$$\gamma_{ex} = - \frac{3 \left[(1+2\beta_3) - (1-\beta_3) \frac{r_{in}^3}{r_{ex}^3} \right]}{(2+\beta_1)(1+2\beta_3) - 2(1-\beta_1)(1-\beta_3) \frac{r_{in}^3}{r_{ex}^3}} \quad (68)$$

Again, subscript ex in γ_{ex} indicates the exterior interface.

In a similar manner, the r component of the electric fields at the interior interface are represented as

$$\mathcal{E}_{kr}(r_{in}, \theta, t) = \frac{1}{2} [\alpha_{k,in} e^{-i\omega t} + \alpha_{k,in}^* e^{i\omega t}] E_0 \cos \theta \quad (69)$$

for $k = 2$ and 3 where subscripts 2 and 3 indicate the electric fields on the membrane side and the interior solution side of the interior interface. The in subscripts in $\alpha_{2,in}$ and $\alpha_{3,in}$ indicate the interior

interface. $\alpha_{2,in}$ and $\alpha_{3,in}$ are represented as

$$\alpha_{2,in} = \frac{9}{(2+\beta_1)(1+2\beta_3) - 2(1-\beta_1)(1-\beta_3) \frac{r_{in}^3}{r_{ex}^3}} \quad (70)$$

$$\alpha_{3,in} = \frac{9\beta_3}{(2+\beta_1)(1+2\beta_3) - 2(1-\beta_1)(1-\beta_3) \frac{r_{in}^3}{r_{ex}^3}} \quad (71)$$

The θ component of the electric fields at the interior interface is written as

$$\mathcal{E}_{\theta}(r_{in}, \theta, t) = \frac{1}{2} [\gamma_{in} e^{-i\omega t} + \gamma_{in}^* e^{i\omega t}] E_0 \sin \theta \quad (72)$$

with

$$\gamma_{in} = - \frac{9\beta_3}{(2+\beta_1)(1+2\beta_3) - 2(1-\beta_1)(1-\beta_3) \frac{r_{in}^3}{r_{ex}^3}} \quad (73)$$

The in subscripts in γ_{in} indicate the interior interface.

The general form of the electrostatic Maxwell stress is shown in eq 16. Among the six independent components of the Maxwell stress tensor in each medium, only rr and $r\theta$ components are important. The rr and $r\theta$ components of the Maxwell stress tensors are represented as

$$T_{krr}(r, \theta, t) = \epsilon_k \left[\frac{1}{2} \mathcal{E}_{kr}^2(r, \theta, t) - \frac{1}{2} \mathcal{E}_{k\theta}^2(r, \theta, t) \right] \quad (74)$$

$$T_{kr\theta}(r, \theta, t) = \epsilon_k E_{kr}(r, \theta, t) E_{k\theta}(r, \theta, t) \quad (75)$$

respectively, with $k = 1, 2$, and 3 . The first suffix k in T_{krr} and $T_{kr\theta}$ represents the medium through which the Maxwell stresses are applied, and the latter two suffixes, rr and $r\theta$, represent the corresponding bases of the tensor components. Because ϕ components are absent from the electric fields, the $r\phi$ and $\theta\phi$ components of the Maxwell stress tensors are zero. The $\theta\theta$ and $\phi\phi$ components of the Maxwell stress tensors are nonzero, but we omit the expressions because those components do not apply net force densities to the vesicle.

The rr and $r\theta$ components of the Maxwell stresses are calculated by eqs 74 and 75, respectively. The rr components of the Maxwell stress tensors on the external solution side, $T_{1rr}(r_{ex}, \theta, t)$, and the membrane side, $T_{2rr}(r_{ex}, \theta, t)$, of the exterior interfaces are represented as

$$\begin{aligned} T_{1rr}(r_{ex}, \theta, t) &= \frac{1}{4} \epsilon_1 E_0^2 \left[\left(|\alpha_{1,ex}|^2 + \frac{\alpha_{1,ex}^2 e^{-i2\omega t} + \alpha_{1,ex}^{*2} e^{i2\omega t}}{2} \right) \cos^2 \theta \right. \\ &\quad \left. - \left(|\gamma_{ex}|^2 + \frac{\gamma_{ex}^2 e^{-i2\omega t} + \gamma_{ex}^{*2} e^{i2\omega t}}{2} \right) \sin^2 \theta \right] \end{aligned} \quad (76)$$

$$\begin{aligned} T_{2rr}(r_{ex}, \theta, t) &= \frac{1}{4} \epsilon_2 E_0^2 \left[\left(|\alpha_{2,ex}|^2 + \frac{\alpha_{2,ex}^2 e^{-i2\omega t} + \alpha_{2,ex}^{*2} e^{i2\omega t}}{2} \right) \cos^2 \theta \right. \\ &\quad \left. - \left(|\gamma_{ex}|^2 + \frac{\gamma_{ex}^2 e^{-i2\omega t} + \gamma_{ex}^{*2} e^{i2\omega t}}{2} \right) \sin^2 \theta \right] \end{aligned} \quad (77)$$

The $r\theta$ components of the Maxwell stresses on the external solution side and the membrane side of the exterior interfaces

are written as

$$T_{1r\theta}(r_{\text{ex}}, \theta, t) = \frac{1}{4} \varepsilon_1 E_0^2 \sin \theta \cos \theta [\alpha_{1,\text{ex}} \gamma_{\text{ex}}^* + \alpha_{1,\text{ex}}^* \gamma_{\text{ex}} + \alpha_{1,\text{ex}} \gamma_{\text{ex}} e^{-i2\omega t} + \alpha_{1,\text{ex}}^* \gamma_{\text{ex}}^* e^{i2\omega t}] \quad (78)$$

$$T_{2r\theta}(r_{\text{ex}}, \theta, t) = \frac{1}{4} \varepsilon_2 E_0^2 \sin \theta \cos \theta [\alpha_{2,\text{ex}} \gamma_{\text{ex}}^* + \alpha_{2,\text{ex}}^* \gamma_{\text{ex}} + \alpha_{2,\text{ex}} \gamma_{\text{ex}} e^{-i2\omega t} + \alpha_{2,\text{ex}}^* \gamma_{\text{ex}}^* e^{i2\omega t}] \quad (79)$$

In a similar manner, the rr components of the Maxwell stress tensors on the membrane side and internal solution side of the interior interfaces are derived as

$$T_{2rr}(r_{\text{in}}, \theta, t) = \frac{1}{4} \varepsilon_2 E_0^2 \left[\left(|\alpha_{2,\text{in}}|^2 + \frac{\alpha_{2,\text{in}}^2 e^{-i2\omega t} + \alpha_{2,\text{in}}^{*2} e^{i2\omega t}}{2} \right) \cos^2 \theta - \left(|\gamma_{\text{in}}|^2 + \frac{\gamma_{\text{in}}^2 e^{-i2\omega t} + \gamma_{\text{in}}^{*2} e^{i2\omega t}}{2} \right) \sin^2 \theta \right] \quad (80)$$

$$T_{3rr}(r_{\text{in}}, \theta, t) = \frac{1}{4} \varepsilon_3 E_0^2 \left[\left(|\alpha_{3,\text{in}}|^2 + \frac{\alpha_{3,\text{in}}^2 e^{-i2\omega t} + \alpha_{3,\text{in}}^{*2} e^{i2\omega t}}{2} \right) \cos^2 \theta - \left(|\gamma_{\text{in}}|^2 + \frac{\gamma_{\text{in}}^2 e^{-i2\omega t} + \gamma_{\text{in}}^{*2} e^{i2\omega t}}{2} \right) \sin^2 \theta \right] \quad (81)$$

The $r\theta$ components of the Maxwell stress tensors on the membrane side and internal solution side of the interior interfaces are expressed as

$$T_{2r\theta}(r_{\text{in}}, \theta, t) = \frac{1}{4} \varepsilon_2 E_0^2 \sin \theta \cos \theta [\alpha_{2,\text{in}} \gamma_{\text{in}}^* + \alpha_{2,\text{in}}^* \gamma_{\text{in}} + \alpha_{2,\text{in}} \gamma_{\text{in}} e^{-i2\omega t} + \alpha_{2,\text{in}}^* \gamma_{\text{in}}^* e^{i2\omega t}] \quad (82)$$

$$T_{3r\theta}(r_{\text{in}}, \theta, t) = \frac{1}{4} \varepsilon_3 E_0^2 \sin \theta \cos \theta [\alpha_{3,\text{in}} \gamma_{\text{in}}^* + \alpha_{3,\text{in}}^* \gamma_{\text{in}} + \alpha_{3,\text{in}} \gamma_{\text{in}} e^{-i2\omega t} + \alpha_{3,\text{in}}^* \gamma_{\text{in}}^* e^{i2\omega t}] \quad (83)$$

By taking the average of the components of the Maxwell stresses, the time-independent parts of the Maxwell stresses at the exterior interfaces are extracted as

$$T_{1rr}(r_{\text{ex}}, \theta) \equiv \langle T_{1rr}(r_{\text{ex}}, \theta, t) \rangle = \frac{1}{4} \varepsilon_1 E_0^2 [|\alpha_{1,\text{ex}}|^2 \cos^2 \theta - |\gamma_{\text{ex}}|^2 \sin^2 \theta] \quad (84)$$

$$T_{2rr}(r_{\text{ex}}, \theta) \equiv \langle T_{2rr}(r_{\text{ex}}, \theta, t) \rangle = \frac{1}{4} \varepsilon_2 E_0^2 [|\alpha_{2,\text{ex}}|^2 \cos^2 \theta - |\gamma_{\text{ex}}|^2 \sin^2 \theta] \quad (85)$$

$$T_{1r\theta}(r_{\text{ex}}, \theta) \equiv \langle T_{1r\theta}(r_{\text{ex}}, \theta, t) \rangle = \frac{1}{4} \varepsilon_1 E_0^2 \sin \theta \cos \theta [\alpha_{1,\text{ex}} \gamma_{\text{ex}}^* + \alpha_{1,\text{ex}}^* \gamma_{\text{ex}}] \quad (86)$$

$$T_{2r\theta}(r_{\text{ex}}, \theta) \equiv \langle T_{2r\theta}(r_{\text{ex}}, \theta, t) \rangle = \frac{1}{4} \varepsilon_2 E_0^2 \sin \theta \cos \theta [\alpha_{2,\text{ex}} \gamma_{\text{ex}}^* + \alpha_{2,\text{ex}}^* \gamma_{\text{ex}}] \quad (87)$$

where $\langle \rangle$ represents the time average over one period of the ac electric field. We denote the time-independent part of the Maxwell stresses $\mathbf{T}_k(r, \theta, t)$ by removing the t dependence from the notation

(i.e., by $\mathbf{T}_k(r, \theta)$ with $k = 1, 2$, and 3). The time-independent part of the Maxwell stresses at the interior interfaces is calculated in a similar manner as

$$T_{2rr}(r_{\text{in}}, \theta) = \frac{1}{4} \varepsilon_2 E_0^2 [|\alpha_{2,\text{in}}|^2 \cos^2 \theta - |\gamma_{\text{in}}|^2 \sin^2 \theta] \quad (88)$$

$$T_{3rr}(r_{\text{in}}, \theta) = \frac{1}{4} \varepsilon_3 E_0^2 [|\alpha_{3,\text{in}}|^2 \cos^2 \theta - |\gamma_{\text{in}}|^2 \sin^2 \theta] \quad (89)$$

$$T_{2r\theta}(r_{\text{in}}, \theta) = \frac{1}{4} \varepsilon_2 E_0^2 \sin \theta \cos \theta [\alpha_{2,\text{in}} \gamma_{\text{in}}^* + \alpha_{2,\text{in}}^* \gamma_{\text{in}}] \quad (90)$$

$$T_{3r\theta}(r_{\text{in}}, \theta) = \frac{1}{4} \varepsilon_3 E_0^2 \sin \theta \cos \theta [\alpha_{3,\text{in}} \gamma_{\text{in}}^* + \alpha_{3,\text{in}}^* \gamma_{\text{in}}] \quad (91)$$

The force densities arising from the Maxwell stresses are calculated by eqs 19 and 20. The work done by the force densities is derived in eq 21 as

$$W_{\text{el}} = W_{\perp} + W_{\parallel} \quad (92)$$

with

$$W_{\perp} = \frac{2\pi}{15} r_{\text{ex}}^2 s E_0^2 [\varepsilon_1 |\alpha_{1,\text{ex}}|^2 - \varepsilon_2 |\alpha_{2,\text{ex}}|^2] + \frac{2\pi}{15} r_{\text{in}}^2 s E_0^2 [\varepsilon_2 |\alpha_{2,\text{in}}|^2 - \varepsilon_3 |\alpha_{3,\text{in}}|^2] + \frac{2\pi}{15} r_{\text{ex}}^2 s E_0^2 (\varepsilon_1 - \varepsilon_2) |\gamma_{\text{ex}}|^2 + \frac{2\pi}{15} r_{\text{in}}^2 s E_0^2 (\varepsilon_2 - \varepsilon_3) |\gamma_{\text{in}}|^2 \quad (93)$$

$$W_{\parallel} = -\frac{2\pi}{15} r_{\text{ex}}^2 s E_0^2 [\varepsilon_1 (\gamma_{\text{ex}} \alpha_{1,\text{ex}}^* + \gamma_{\text{ex}}^* \alpha_{1,\text{ex}}) - \varepsilon_2 (\gamma_{\text{ex}} \alpha_{2,\text{ex}}^* + \gamma_{\text{ex}}^* \alpha_{2,\text{ex}})] - \frac{2\pi}{15} r_{\text{in}}^2 s E_0^2 [\varepsilon_2 (\gamma_{\text{in}} \alpha_{2,\text{in}}^* + \gamma_{\text{in}}^* \alpha_{2,\text{in}}) - \varepsilon_3 (\gamma_{\text{in}} \alpha_{3,\text{in}}^* + \gamma_{\text{in}}^* \alpha_{3,\text{in}})] \quad (94)$$

by the first-order terms of s . Note that the lowest-order terms of W_{el} with respect to s are linear in s .

Appendix C: Expressions for Coefficients A , B , and C in Equation 37.

The morphological transitions are indicated by zeros of the work done by the Maxwell stresses W_{el} . $\Lambda(\bar{\omega})$ (eq 40) is the determinant of the zeros of W_{el} . $\Lambda(\bar{\omega})$ is a quadratic function of $\bar{\omega}^2$. The number of zeros in W_{el} is determined by the sign and the magnitude of coefficients A , B , and C . Here, we summarize the dependence of A , B , and C on the conductivities and the dielectric constants of the membrane and the two solutions, as well as on the vesicle geometry. For simplicity, we assume that the dielectric constants are symmetric across the membrane (i.e., $\varepsilon_{\text{ex}} = \varepsilon_{\text{in}} = \varepsilon_{\text{w}}$) and that the conductivities are asymmetric (i.e., $\sigma_{\text{ex}} \neq \sigma_{\text{in}}$).

A is represented as

$$A = -\frac{\varepsilon_{\text{me}}}{\varepsilon_{\text{w}}} \left(1 - \frac{\varepsilon_{\text{me}}}{\varepsilon_{\text{w}}} \right) \left[\left(1 + 2 \frac{\varepsilon_{\text{me}}}{\varepsilon_{\text{w}}} \right) + 2 \left(\frac{r_{\text{in}}}{r_{\text{ex}}} \right)^3 \left(1 - \frac{\varepsilon_{\text{me}}}{\varepsilon_{\text{w}}} \right) \right]^2 + \left(1 - \frac{\varepsilon_{\text{me}}}{\varepsilon_{\text{w}}} \right) \left[\left(1 + 2 \frac{\varepsilon_{\text{me}}}{\varepsilon_{\text{w}}} \right) - \left(\frac{r_{\text{in}}}{r_{\text{ex}}} \right)^3 \left(1 - \frac{\varepsilon_{\text{me}}}{\varepsilon_{\text{w}}} \right) \right]^2 + 9 \left(\frac{r_{\text{in}}}{r_{\text{ex}}} \right)^2 \frac{\varepsilon_{\text{me}}}{\varepsilon_{\text{w}}} \left(1 - \frac{\varepsilon_{\text{me}}}{\varepsilon_{\text{w}}} \right)^2 \quad (95)$$

A is independent of the conductivities of the solutions and the membrane, σ_{ex} , σ_{me} , and σ_{in} . A is plotted as a function of $r_{\text{in}}/r_{\text{ex}}$ for several $\varepsilon_{\text{me}}/\varepsilon_{\text{w}}$ values in Figure 8. A values with typical dielectric constants of the membrane, $\varepsilon_{\text{me}} \approx 2\varepsilon_0$, and water, $\varepsilon_{\text{w}} \approx 78\varepsilon_0$, are plotted with the solid curve in Figure 8. A is positive for all radius ratios $r_{\text{in}}/r_{\text{ex}}$ for the dielectric constants studied. In the limit of

vanishing membrane thickness, $r_{in}/r_{ex} \rightarrow 1$, A is zero. Because the thickness of the giant vesicles is much smaller than the radius, $r_{in}/r_{ex} = 1 - \delta \approx 1$, A is a very small positive value for the vesicles studied in the experiments. For comparison, the graphs of A are plotted for $\epsilon_{me}/\epsilon_w = 0.013$ and 0.051 with the dotted and broken curves in Figure 8, respectively. A is not strongly sensitive to the dielectric constants of the membrane and the solutions.

B is represented in the form of a quadratic function of χ as

$$B = b_2\chi^2 + b_1\chi + b_0 \quad (96)$$

with

$$b_2 = -\frac{\epsilon_{me}}{\epsilon_w} \left(1 - \frac{\epsilon_{me}}{\epsilon_w}\right) \left(1 + 2\left(\frac{r_{in}}{r_{ex}}\right)^3\right)^2 + \left(1 - \frac{\epsilon_{me}}{\epsilon_w}\right) \left(1 - \left(\frac{r_{in}}{r_{ex}}\right)^3\right)^2 + 9\frac{\epsilon_{me}}{\epsilon_w} \left(\frac{r_{in}}{r_{ex}}\right)^2 \quad (97)$$

$$b_1 = 2\left(1 - \frac{\epsilon_{me}}{\epsilon_w}\right) \left(1 - \left(\frac{r_{in}}{r_{ex}}\right)^3\right) \frac{\sigma_{me}}{\sigma_{ex}} \left(2 + \left(\frac{r_{in}}{r_{ex}}\right)^3\right) - 2\frac{\epsilon_{me}}{\epsilon_w} \left(1 + 2\left(\frac{r_{in}}{r_{ex}}\right)^3\right) - 18\left(\frac{r_{in}}{r_{ex}}\right)^3 \frac{\epsilon_{me}}{\epsilon_w} \left(\frac{\sigma_{me}}{\sigma_{ex}} - \frac{\epsilon_{me}}{\epsilon_w}\right) + 18\left(\frac{r_{in}}{r_{ex}}\right)^2 \left(\frac{\epsilon_{me}}{\epsilon_w}\right) \left(\frac{\sigma_{me}}{\sigma_{ex}}\right) \quad (98)$$

$$b_0 = -4\frac{\epsilon_{me}}{\epsilon_w} \left(1 - \frac{\epsilon_{me}}{\epsilon_w}\right) \left(1 - \left(\frac{r_{in}}{r_{ex}}\right)^3\right)^2 \left(\frac{\sigma_{me}}{\sigma_{ex}}\right)^2 - 27\left(\frac{r_{in}}{r_{ex}}\right)^2 \left(\frac{\sigma_{me}}{\sigma_{ex}}\right)^2 + \left(1 - \frac{\epsilon_{me}}{\epsilon_w}\right) \left(2 + \left(\frac{r_{in}}{r_{ex}}\right)^3\right)^2 \left(\frac{\sigma_{me}}{\sigma_{ex}}\right)^2 + 9\left(\frac{r_{in}}{r_{ex}}\right)^2 \frac{\epsilon_{me}}{\epsilon_w} \left(1 - \frac{\epsilon_{me}}{\epsilon_w}\right) + \left(\left(\frac{\sigma_{me}}{\sigma_{ex}}\right)^2 - \frac{\epsilon_{me}}{\epsilon_w}\right) \left[\left(1 + 2\frac{\epsilon_{me}}{\epsilon_w}\right) + 2\left(\frac{r_{in}}{r_{ex}}\right)^3 \left(1 - \frac{\epsilon_{me}}{\epsilon_w}\right) \right]^2 + \left(1 - \frac{\epsilon_{me}}{\epsilon_w}\right) \left[\left(1 + 2\frac{\epsilon_{me}}{\epsilon_w}\right) - \left(\frac{r_{in}}{r_{ex}}\right)^3 \left(1 - \frac{\epsilon_{me}}{\epsilon_w}\right) \right]^2 + 2\left(\frac{\sigma_{me}}{\sigma_{ex}} - \frac{\epsilon_{me}}{\epsilon_w}\right) \left[\left(1 + 2\frac{\epsilon_{me}}{\epsilon_w}\right) + 2\left(\frac{r_{in}}{r_{ex}}\right)^3 \left(1 - \frac{\epsilon_{me}}{\epsilon_w}\right) \right] + 2\left(\frac{r_{in}}{r_{ex}}\right)^3 \left(1 - \frac{\epsilon_{me}}{\epsilon_w}\right) \right] \times \left[\left(1 + 2\frac{\epsilon_{me}}{\epsilon_w}\right) - \left(\frac{r_{in}}{r_{ex}}\right)^3 \left(1 - \frac{\epsilon_{me}}{\epsilon_w}\right) \right] + 9\left(\frac{r_{in}}{r_{ex}}\right)^3 \frac{\sigma_{me}}{\sigma_{ex}} \quad (99)$$

The B values are plotted as a function of χ for several ϵ_{me}/ϵ_w values in Figure 9a, where $r_{in}/r_{ex} = 0.999$ and $\sigma_{me}/\sigma_{ex} = 0$. Typical values of the dielectric constants of lipid membrane, $\epsilon_{me} = 2\epsilon_0$, and water, $\epsilon_w = 80\epsilon_0$, are used to calculate the solid curves in Figure 9. The graphs of B values for $\epsilon_{me}/\epsilon_w = 0.051$ and 0.013 are also plotted as the dotted and broken curves in Figure 9a for comparison. The sign of B changes at $\chi \approx 1$ for all of the ϵ_{me}/ϵ_w values investigated. B is negative for $\chi < 1$ and is positive for $\chi > 1$. The sign of B changes exactly at $\chi = 1$ for vanishing membrane thickness (i.e., $r_{in}/r_{ex} = 1$). B is plotted as a function of χ for several r_{in}/r_{ex} values and $\sigma_{me}/\sigma_{ex} = 0$ in Figure 9b, where ϵ_{me}/ϵ_w and σ_{me}/σ_{ex} are fixed to 0.026 . The solid curves in Figure 9a–c are plotted for identical parameters. r_{in}/r_{ex} is represented as $1 - (l_{me}/r_{ex})$ and increases with the radius of the vesicle. The χ value at which B changes sign shifts to a smaller value

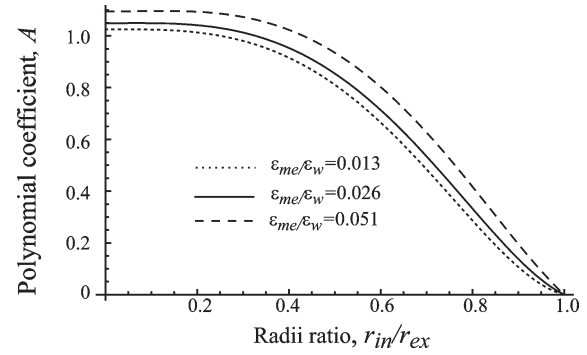


Figure 8. Plots of the coefficient A of the polynomial $\Lambda(\bar{\omega})$ defined by eq 37 as a function of the ratio r_{in}/r_{ex} between the interior and exterior radii. The dotted, solid, and broken curves are plotted for the dielectric constant ratio ϵ_{me}/ϵ_w between the membrane and water: 0.013, 0.026, and 0.051, respectively.

as r_{in}/r_{ex} becomes smaller. If the vesicle is very thick or very small, in particular, if the thickness is larger than about 3% of the radius of the vesicle, then B is positive for the entire range of χ . B is plotted as a function of χ for several σ_{me}/σ_{ex} values in Figure 9c, where ϵ_{me}/ϵ_w and r_{in}/r_{ex} are fixed to 0.026 and 0.999 , respectively. Because the conductivity of pure water is on the order of 10^{-5} S/m (i.e., σ_{me}/σ_{ex} is smaller than 10^{-9} for lipid membranes), $\sigma_{me}/\sigma_{ex} \approx 0$ is a good approximation even in the absence of salt in the solution. The B values of the vesicles change sign at $x \approx 1$ for $\sigma_{me}/\sigma_{ex} \approx 0$, where B is negative for $x < 1$ and is positive for $x > 1$. The dependence of the χ value on σ_{me}/σ_{ex} , at which B changes sign, is negligibly small at least in the σ_{me}/σ_{ex} range of interest (i.e., $10^{-11} \leq \sigma_{me}/\sigma_{ex} \leq 10^{-9}$). For a spherical shell made of conducting material with large σ_{me}/σ_{ex} (e.g., Figure 9c), B is positive for all χ values.

The expression for C is written in the form of a quadratic function of χ and is given as

$$C = c_2\chi^2 + c_1\chi + c_0 \quad (100)$$

with

$$c_2 = \left(\frac{\sigma_{me}}{\sigma_{ex}} \left(1 + 2\left(\frac{r_{in}}{r_{ex}}\right)^3\right) + \left(1 - \left(\frac{r_{in}}{r_{ex}}\right)^3\right) \right)^2 - \frac{\epsilon_{me}}{\epsilon_w} \left(2 + \left(\frac{r_{in}}{r_{ex}}\right)^3\right)^2 + 9\frac{\epsilon_{me}}{\epsilon_w} \left(\frac{r_{in}}{r_{ex}}\right)^2 \quad (101)$$

$$c_1 = 2\frac{\sigma_{me}}{\sigma_{ex}} \left[\left(\left(1 - \left(\frac{r_{in}}{r_{ex}}\right)^3\right) + \frac{\sigma_{me}}{\sigma_{ex}} \left(1 + 2\left(\frac{r_{in}}{r_{ex}}\right)^3\right) \right) \times \left(2\frac{\sigma_{me}}{\sigma_{ex}} \left(1 - \left(\frac{r_{in}}{r_{ex}}\right)^3\right) + \left(2 + \left(\frac{r_{in}}{r_{ex}}\right)^3\right) \right) - \frac{\epsilon_{me}}{\epsilon_w} \left(2 + \left(\frac{r_{in}}{r_{ex}}\right)^3\right) \left(4 - \left(\frac{r_{in}}{r_{ex}}\right)^3\right) + 9\frac{\epsilon_{me}}{\epsilon_w} \left(\frac{r_{in}}{r_{ex}}\right)^2 \right] \quad (102)$$

$$c_0 = \left(\frac{\sigma_{me}}{\sigma_{ex}}\right)^2 \left[\left(2\frac{\sigma_{me}}{\sigma_{ex}} \left(1 - \left(\frac{r_{in}}{r_{ex}}\right)^3\right) + \left(2 + \left(\frac{r_{in}}{r_{ex}}\right)^3\right) \right)^2 - \frac{\epsilon_{me}}{\epsilon_w} \left(4 - \left(\frac{r_{in}}{r_{ex}}\right)^3\right)^2 + 9\left(\frac{r_{in}}{r_{ex}}\right)^2 \left(\frac{\epsilon_{me}}{\epsilon_w} - 2\right) - 18\left(\frac{r_{in}}{r_{ex}}\right)^2 \right] \quad (103)$$

Coefficients c_1 and c_0 are composed of terms proportional to σ_{me}/σ_{ex} and $(\sigma_{me}/\sigma_{ex})^2$, and it is possible to assume $c_1 \approx 0$ and $c_0 \approx 0$ for

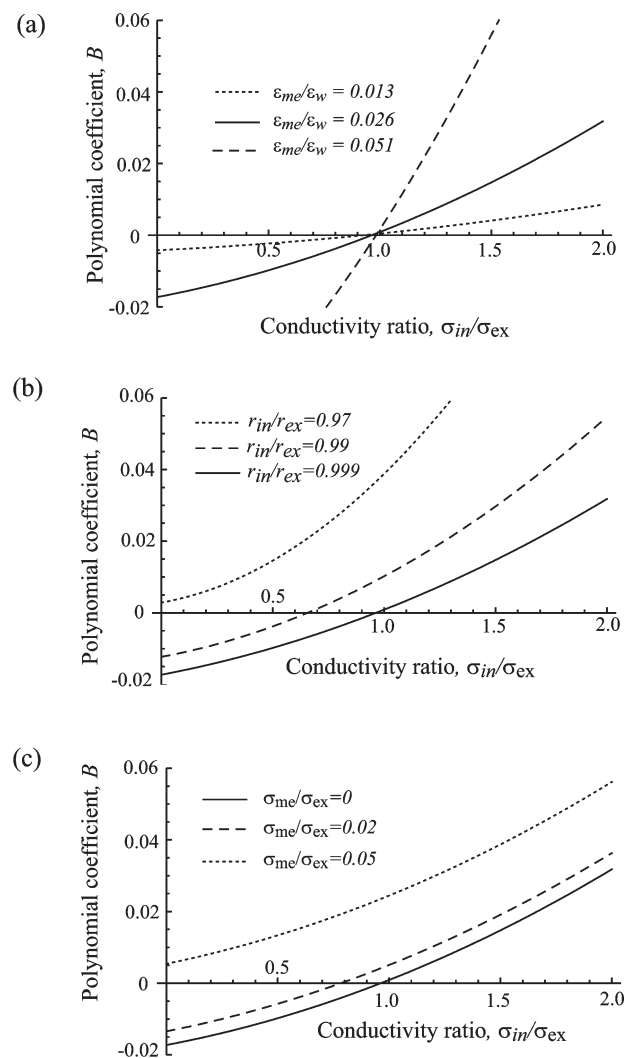


Figure 9. B coefficients of $\Lambda(\bar{\omega})$, defined in eq 37, plotted as a function of the conductivity ratio σ_{in}/σ_{ex} between the interior and the exterior solutions. (a) Plots of B for several values of the dielectric constant ratio ϵ_{me}/ϵ_w between the membrane and water. The dotted, solid, and broken curves are plotted for $\epsilon_{me}/\epsilon_w = 0.013$, 0.026 , and 0.051 , respectively. The r_{in}/r_{ex} ratio between the interior and exterior radii is fixed to 0.999 , and the conductivity ratio between the membrane and the exterior solutions is fixed to 0 . (b) Plots of B for $\epsilon_{me}/\epsilon_w = 0.026$, $\sigma_{me}/\sigma_{ex} = 0$, and several r_{in}/r_{ex} values. The r_{in}/r_{ex} values used to plot the dotted, broken, and solid curves are 0.97 , 0.99 , and 0.999 , respectively. (c) Plots of B for $r_{in}/r_{ex} = 0.999$, $\epsilon_{me}/\epsilon_w = 0.026$, and several σ_{me}/σ_{ex} values. The σ_{me}/σ_{ex} values used to plot the solid curve, the broken curve, and the dotted curve are 0 , 0.02 , and 0.05 , respectively.

the experimental conditions under which $\sigma_{me}/\sigma_{ex} \approx 0$ is a good approximation. The values of C are calculated as a function of χ for several ϵ_{me}/ϵ_w values in Figure 10a, where r_{in}/r_{ex} and σ_{me}/σ_{ex} are fixed to 0.999 and 0 , respectively. The solid curve in Figure 10a is plotted for a typical dielectric constant of the lipid membrane, $\epsilon_{me} = 2\epsilon_0$, and water, $\epsilon_w = 78\epsilon_0$ (i.e., $\epsilon_{me}/\epsilon_w = 0.026$). For vanishing σ_{me}/σ_{ex} , C is positive for the entire range of χ values. For comparison, C is also plotted for $\epsilon_{me}/\epsilon_w = 0.013$ and $\epsilon_{me}/\epsilon_w = 0.051$ with the dotted and broken curves in Figure 10a, respectively. These plots show that C is not strongly sensitive to the dielectric constants. The C values are plotted as a function of χ for several r_{in}/r_{ex} values in Figure 10b, and ϵ_{me}/ϵ_w and σ_{me}/σ_{ex} are fixed to 0.026 and 0 , respectively. The solid lines in Figure 10a–c are plotted for identical parameters. The solid lines in Figure 10b,c

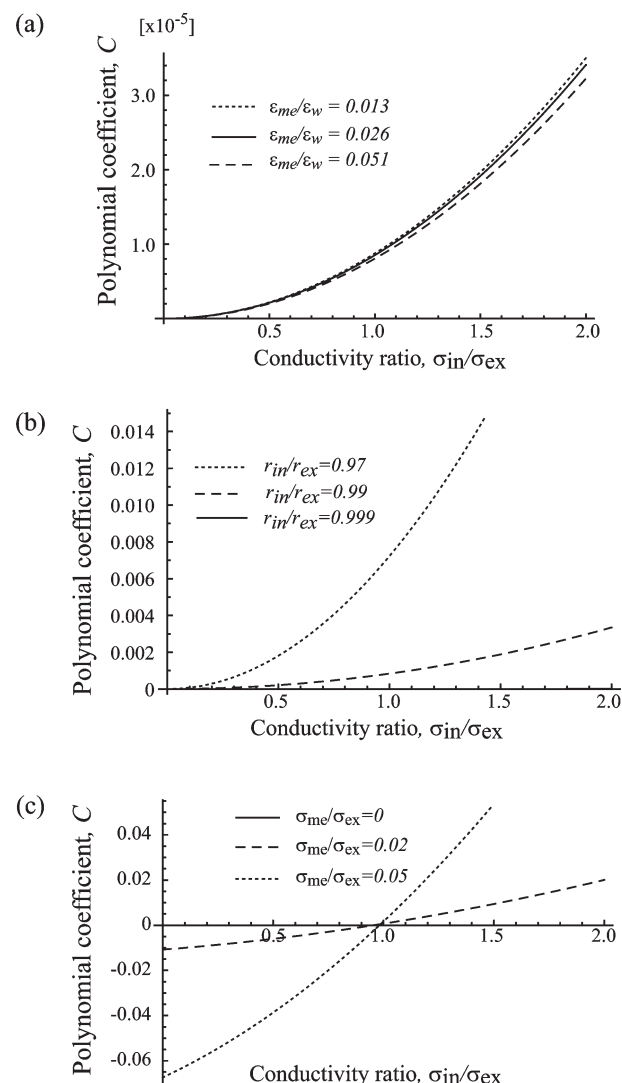


Figure 10. Coefficient C of $\Lambda(\bar{\omega})$, defined in eq 37, plotted as a function of the conductivity ratio σ_{in}/σ_{ex} between the interior and the exterior solutions. (a) Plots of C for several values of the dielectric constant ratio ϵ_{me}/ϵ_w between the membrane and water. The ϵ_{me}/ϵ_w values used to plot the dotted, solid, and broken curves are 0.013 , 0.026 , and 0.051 , respectively. The ratio r_{in}/r_{ex} of the interior and exterior radii is fixed to 0.999 , and the conductivity ratio σ_{me}/σ_{ex} is fixed to 0 . (b) Plots of C for $\epsilon_{me}/\epsilon_w = 0.026$, $\sigma_{me}/\sigma_{ex} = 0$, and for several r_{in}/r_{ex} values. The dotted, broken, and solid curves are plotted for $r_{in}/r_{ex} = 0.97$, $r_{in}/r_{ex} = 0.99$, and $r_{in}/r_{ex} = 0.999$, respectively. (c) Plots of C for $r_{in}/r_{ex} = 0.999$, $\epsilon_{me}/\epsilon_w = 0.026$, and several values of σ_{me}/σ_{ex} . The σ_{me}/σ_{ex} values used to plot the solid, broken, and dotted curves are 0 , 0.02 , and 0.05 , respectively.

almost overlap with the χ axis at first glance because the C values for this condition are much smaller than those for the other conditions. The ratio r_{in}/r_{ex} increases with the vesicle radius, and Figure 10b shows that C values increase with the membrane thickness. C is sensitive to r_{in}/r_{ex} to some extent. For vanishing σ_{me}/σ_{ex} , the values of C are always positive for the entire range of χ and r_{in}/r_{ex} . C is plotted as a function of χ for several σ_{me}/σ_{ex} values in Figure 10, where ϵ_{me}/ϵ_w and r_{in}/r_{ex} are fixed to 0.026 and 0.999 , respectively. Conductivities σ_{ex} and σ_{in} are changed systematically in the range from 10^{-5} to 10^{-3} in the experiments; however, the C values did not show a noticeable change in the range of σ_{me}/σ_{ex} values of interest. If the vesicle were made of conducting material so that σ_{me}/σ_{ex} were larger than 0.02 , C would change sign at about $\chi = 1$.

In summary, for typical experimental parameters, A and C are positive and take small values for all χ values. B changes sign at about $\chi = 1$, where $B < 0$ for $\chi < 1$ and $B > 0$ for $\chi > 1$. These properties originate from the fact that lipid bilayer membranes behave as insulators and that the thickness of the bilayer membrane is much smaller than the lateral dimension of the vesicle. The morphological transitions predicted from these properties are described in section 5. The present model is applicable to thick membranes (e.g., polymer capsules or polymersomes).⁴⁵ For the thick membranes, A and C are still positive but take larger values than those for lipid bilayer membranes. B is positive for the whole range of χ values if the thickness of the membrane exceeds about 3% of the radius of the object. In this limit, the prolate–oblate

transitions are truncated. For the spherical shell made of conducting materials, A is still positive but the behaviors of B and C change dramatically. C changes sign at about $\chi = 1$ for large $\sigma_{\text{me}}/\sigma_{\text{ex}}$ (e.g., 0.02). B changes sign at some value smaller than $\chi = 1$ for $\sigma_{\text{me}}/\sigma_{\text{ex}}$ values smaller than 0.05. However, B is positive for the entire range of χ for $\sigma_{\text{me}}/\sigma_{\text{ex}}$ larger than 0.05.

Supporting Information Available: List of the symbols

- . Physical constants
- . Bending energies required for prolate/oblate deformation.
- Quasistatic Maxwell equations and Maxwell–Wagner theory
- . Brief derivation of eqs 42 and 43
- . This material is available free of charge via the Internet at <http://pubs.acs.org>.

(45) Discher, B. M.; Won, Y. Y.; Ege, D. S.; Lee, J. C. M.; Bates, F. S.; Discher, D. E.; Hammer, D. A. *Science* **1999**, 284, 1143–1146.